Bistatic Analysis Using the Real Representation Scattering Matrix Eigen-Classification

Madalina Ciuca, Gabriel Vasile, Andrei Anghel, Michel Gay, Silviu Ciochina

Bistatic Analysis using the Real Representation Scattering Matrix Eigen-classification

Madalina Ciuca*† *Student Member, IEEE*, Gabriel Vasile* , *Senior Member, IEEE*, Andrei Anghel† , *Senior Member, IEEE*, Michel Gay* , *Senior Member, IEEE*, and Silviu Ciochina † , *Senior Member, IEEE*

***Abstract*—Exploring polarimetric diversity of Synthetic Aperture Radar (SAR) data is directly applicable to conventional monostatic cases. For this, the mostly used convention is the Backscatter Alignment. While establishing important advantages for the monostatic case (possibility to have equal values on the cross-polarimetric channels), it has been proven to introduce some difficulties for the bistatic case. This appears in relation to the so-called conjugate similarity operation, when (mathematically) asymmetric scattering matrices occur. In this paper, we propose the detailed algorithm which provides a solution to the conjugate similarity operation, in the case of general scattering matrices. The proposed algorithm is based on the real representation matrix transformation. Further, we investigate the characterization of canonical bistatic scatterers (three elementary targets). Raw bistatic polarimetric signals are obtained by using simulations with a computationally electromagnetic (EM) software, capable of complete EM analysis. The eigenvalue classification illustrates the potential of additional information brought using the proposed Real Representation Scattering Matrix (RRSM). The presence of complex eigenvalues is investigated in relation to the bistatic angle and one nonreciprocity parameter.**

***Index Terms*—Real representation, scattering matrix, polarimetry, bistatic, consimilarity, conjugate similarity, nonreciprocity factor, full-polarimetric, computational electromagnetic.**

I. Introduction

In radar polarimetry, the scattering matrix, $\mathbf{S} \in \mathbf{C}^{2\times 2}$, of coherent targets, completely describes the transformations occurred to the incident electric field during the scattering phenomenon.

In compliance with IEEE standards, the polarization is an antenna property and the scattering process in radar is often described considering a so-called "antenna oriented" convention. In the framework of this convention, compared to the optical one, the scattered versor is geometrically oriented as from the antenna to the target, i.e., a reversal of 180^o from the general right-handed geometric description [1]. This is known as the Backscatter Alignment (BSA), while the more common coordinate system used in optics goes under the name of Forward Scattering Alignment (FSA) [2]. The geometrical representations for BSA and FSA will not be included here, but the interested reader can consult texts as [1], [2].

Because in radar theory, the vector on the receiver path is reversed in direction, this will mathematically be modelled by the conjugation operation. In this regard, the basis change relations of the two conventions (radar vs. optical), are slightly different. While the Optical Polarimetry Theory operates with similarity transformations performed on the Jones matrix, the Radar Polarimetry Theory under BSA operates with conjugate similarity transformations performed on the Sinclair matrix. Also an equivalence relation of complex matrices, the con(jugate) similarity differs from the (conventional) similarity operation [3] and we dedicate Subsection III-A for comparing the two.

In practical implementations, under the use of simplifying assumptions, the consimilarity transformation reduces to more particular cases, so this equivalence relation under BSA, has rarely been used in its generalized form. We refer here to the case of all monostatic systems, where the symmetry of the scattering matrix is generally claimed under BSA (i.e, equal values for the cross-polarized elements). This appears as consequence of an equal travel path of the incidence/scattered wave when assuming a medium with unchanged properties between transmitter (Tx) / receiver (Rx) and target (Tg) elements [4]. Such matrix is often referred as a reciprocal scattering matrix, i.e, symmetric in a mathematical

Manuscript received Month Day, Year; revised Month Day, Year.
M. Ciuca is with Laboratoire Grenoble Images Parole Signal Automatique (GIPSA-lab), Univ. Grenoble Alpes, CNRS, Grenoble INP, 38000 Grenoble, France, and with the Department of Telecommunications, University Politehnica of Bucharest, 060032 Bucharest, Romania (email: ileana-madalina.ciuca@grenoble-inp.fr).
G. Vasile is with Laboratoire Grenoble Images Parole Signal Automatique (GIPSA-lab), Univ. Grenoble Alpes, CNRS, Grenoble INP, 38000 Grenoble, France (email: gabriel.vasile@grenoble-inp.fr).
A. Anghel is with Department of Telecommunications, Research Center for Spatial Information, University Politehnica of Bucharest, 060032 Bucharest, Romania (e-mail: andrei.anghel@munde.pub.ro).
M. Gay is with Laboratoire Grenoble Images Parole Signal Automatique (GIPSA-lab), Univ. Grenoble Alpes, CNRS, Grenoble INP, 38000 Grenoble, France (email: michel.gay@grenoble-inp.fr).
S. Ciochina is with Department of Telecommunications, University Politehnica of Bucharest, 060032 Bucharest, Romania (e-mail: silviu@comm.pub.ro).

sense. Under the reciprocity simplification, the general conjugate similarity operation transforms to a so-called unitary congruence transformation [5].

For extracting descriptive parameters directly from a scattering matrix, coherent decomposition techniques are used. The coherent decomposition of nonreciprocal scattering matrices has been investigated in the literature using the Singular Value Decomposition (SVD) [6], [7]. This allows one to decompose the scattering matrix by means of two unitary transformations, one characterizing the Tx-Tg path and one the Tg-Rx path. The unitarity of the transformation matrices on each path imposes that the vectors describing the transformation are orthogonal. However, from a physical point of view, different properties of the medium may not allow for preservation of the unitary property of transformation matrices associated to the two paths. With the consimilarity operation, a restriction of the model is that the two transformation matrices on each path are conjugate pairs. According to Lüneburg, the radar polarization vectors (i.e., the columns of the transformation matrix), even if related by a complex conjugation operation (i.e., a change in the sense of rotation), describe the same state of polarization [8].

The SVD method has been introduced specifically for the bistatic case and some well-known coherent models based on a product decomposition have been extended for incorporating this operation. We mention here the extended Kennaugh [9], [10], the Huynen (and Huynen Fork representation) [6], [11]–[13] and the Target Scattering Vector Model (TSVM) [14]. The extension is mathematically justified in all works by the general property that unitary congruence is considered a particular case of SVD.

Here, for a more comprehensive methodology for decomposing the scattering matrix via the con(jugate) similarity operation, irrespective of its compliance with the reciprocity theorem, we propose the use of a real representation scattering matrix (RRSM) computation framework [15]. Some elementary definitions and properties are presented in Section III and Annex B.

One can emphasize that the two mathematical models (SVD and consimilarity) may represent both only particular transformation (considering the constraints discussed above for each case) when dealing with general bistatic representations. While the present work concentrates on the consimilarity relation and will not deal directly with the connection between these two models, with the SVD being currently the de facto method of coherent bistatic radar polarimetry, the comparison was inevitable.

In this paper, we introduce the detailed algorithm for solving the general conjugate similarity transformation for radar. The proposed algorithm is based on the real representation (RR) of scattering matrices.

The RR analysis of four complex matrix types allows us to illustrate some interesting mathematical properties of their associated eigenvalues. In practice, we propose to analyse scattering matrices of elementary targets in the bistatic case. Three canonical scattering targets are simulated, and we explore the connection between nonreciprocity of scattering matrices and RRSM eigenvalues classification.

Throughout the paper $\mathbf{A}^T$, $\mathbf{A}^*$ and $\mathbf{A}^H$ represent the transpose, complex conjugate and complex conjugate transpose operations of a complex matrix ($\mathbf{A} \in \mathbb{C}^{n\times n}$). A matrix is represented in uppercase boldface letters ($\mathbf{A}$) and a vector in lowercase boldface ($\mathbf{a}$) (with accent for unitary vectors, $\hat{\mathbf{a}}$). Operators $\mathrm{Re}(\cdot)$ and $\mathrm{Im}(\cdot)$ are used in extracting the real and imaginary components of any scalar, vector or matrix.

Aside from this introduction, the paper contains four more sections. Section II is dedicated to a state-of-the-art analysis of general bistatic polarimetric practical systems. We mention there both previous implementations, as well as some forthcoming bistatic systems (to present polarimetric capabilities) under development with different spatial companies. While some of these projects are aimed only with partial polarimetric capabilities, they present nonetheless prospects of an increased interest in future bistatic polarimetric missions.

In Section III, we introduce the general definition and particularities of the real representation scattering matrix (RRSM). As one expects to encounter both reciprocal and nonreciprocal scattering matrices in dealing with bistatic polarimetric real scattering scenarios, we consider four particular forms for a complex matrix and discuss the general types of eigenvalues expected for their RRSM. Section IV offers a general overview of the full-wave bistatic simulated results, while conclusions, interpretations and highlights can be found in Section V.

II. Bistatic polarimetry systems - State of art

In a bistatic configuration, the transmitter (Tx) and receiver (Rx) are no longer co-located, but placed in two separate positions. For a fixed target, we define a so-called bistatic angle (β) parameter between the Tx and Rx line-of-sight (LOS) directions. An important advantage of bistatic configurations is the possibility to obtain enhanced or complementary target signatures, compared to monostatic geometries. Combined with a polarimetric diversity, the amount of information acquired by bistatic systems may be significant. Recent years have been fruitful for constructing and exploiting bistatic / multistatic experimental radar designs, leading to the point that, for example, spaceborne-spaceborne configurations with large separation between Tx and Rx elements are at the moment viable projects under implementation.

TABLE I
Extensive list of full-polarimetric bistatic missions and platforms.

Bistatic configuration	Ref.	Tx System (Institution/Campaign)	Rx System (Institution/Campaign)	Acq. Band
Geometries capable of large bistatic angles ($\beta > 10^o$):				
spaceborne-airborne	[16], [17]	TerraSAR-X (DLR)	F-SAR (DLR)	X-Band
spaceborne-groundbased	[18], [19]	TerraSAR-X (DLR)	Hitchhiker (ZESS - University of Siegen)	X-Band
	[20]	ASTRA 1KR, DVB-S(2)	SABBIA (Fraunhofer FHR)	Ku-Band
airborne-groundbased	[21], [22]	Ingara (Australian DSTO)	passive Rx (X-Band)	L & X Bands
groundbased-groundbased	[23]	TARA (TU Delft)	PARSAX (TU Delft)	S-Band
	[24]	KAPRI-Tx (GAMMA Remote Sensing)	KAPRI-Rx (GAMMA Remote Sensing)	Ku-Band
Geometries with smaller bistatic angles ($\beta \leq 10^o$):				
airborne-airborne	[25], [26]	BelSAR (MetaSensing)	BelSAR (MetaSensing)	L-Band
Quasi-monostatic:				
airborne-airborne	[27]	N-SAR (Nanjing Research Institute)	N-SAR	X-Band
groundbased-groundbased	[28]	Tx unit (Tohokun University)	OEFS-Rx (Tohokun University)	C-Band
	[29]	KAPRI-Tx (GAMMA Remote Sensing)	KAPRI-Rx (GAMMA Remote Sensing)	Ku-Band

A. Future planned bistatic satellite missions:

- *Geometries capable of larger bistatic angles:*

  At the European Space Agency (ESA), Harmony (former known as STEREOID) is a mission concept, recently selected as the 10^{th} Earth Explorer Scientific Program and estimated for launch around 2028. The mission will use two passive payloads (Harmony-A and Harmony-B) equipped with radar instruments, which will work in bistatic configuration(s) with one of the Sentinel-1 satellites (to play the role of transmitter) [30] [31]. With at least a 250 km along-track separation between Tx and Rx and considering the current orbit height of the Sentinel-1 satellites of 693 km, the Harmony configuration will allow a minimum of 20^o bistatic angle. Because the transmitter, a Sentinel-1 satellite, ensure only one illuminating polarisation capability in most working modes, the Harmony mission will provide only dual-pol products. Considering the Open-Data policy adopted by ESA, it is expected such products will be available for a great range of applications.
- *Quasi-monostatic and geometries capable of smaller bistatic angles:*

  The TerraSAR-X/TanDEM-X couple has played a pioneering role in the spaceborne area and has demonstrated and confirmed the utility of acquiring radar images with sensors located at different positions. Currently in orbit, due to the small separation between the two platforms compared to their altitude height, they are considered to have only a quasi-monostatic (i.e., nearly monostatic) field of view [32]. Such a geometry presents however, the advantage of using processing algorithms which are only very slightly modified from the monostatic ones [33].
  Under development at DLR, the future HRWS (High Resolution Wide Swath) SAR mission [34] will exploit a monostatic and multistatic functionality, with passive transponder-like companions separated by the main payload by baselines comparable to that of TerraSAR-X/TanDEM-X. As a result, such system will allow low bistatic angles for each Tx-Rx combination. The mission will present also some form of polarimetric diversity: dual or full-pol.

  Another future bistatic mission inspired by the TerraSAR-X/TanDEM-X formation is the LuTan-1 (also as, TwinSAR-L) [35] of the Chinese spatial agency. The L-Band mission is intended to present full-polarisation capability, while the baseline between the two payloads is optimized for interferometric applications and the resulting bistatic angles will be only in the order of several degrees.

B. Inventory of bistatic polarimetric system implementations:

With respect to other already implemented bistatic configurations, there are in the literature examples in a wide range of same/cross-platform configurations: spaceborne-airborne [36], [37], spaceborne-groundbased [38], [39], airborne-airborne [40], [41], airborne-groundbased [42]. However, there have been only a small number of bistatic experiments and campaigns integrating full-polarimetric features. In Table I we present an extensive selection of such systems having different bistatic configurations or working frequencies, and we group them with respect to the bistatic angle separation. We use a threshold value of $\beta = 10^o$ for separating between classes with larger and smaller bistatic angles. In principle, the scattering properties at larger bistatic angles are expected to be different than the ones with monostatic or quasi-monostatic scattering. This has been shown in [43] for different bistatic backscattering measurements of radar cross-sections (RCSs) over the ocean surface. Apart from the two extreme cases, evaluating the scattering around smaller bistatic angles is expected to present intermediate properties. Nonetheless, there is no consensus in the literature regarding an exact threshold value for β.

While we do not claim for Table I to represent an exhaustive indexing of previously/currently available full-polarimetric bistatic platforms, the selections are nonetheless representative examples in the literature. Indoor bistatic experimental facilities or bistatic systems presenting only a dual-polarisation capability have not been included in the table.

III. The real representation of general scattering matrices

Introduced as a pure algebraic concept for performing the more-challenging consimilarity transformation, we have observed that the real representation form presents some interesting properties in terms of its eigenvalue/eigenvector decomposition. Moreover, the type of values may be placed in relation to the nonreciprocity parameter, connection which will also be introduced in this section.

TABLE II
Consimilarity and similarity general equations.

similarity	**con(jugate) similarity**
$\mathbf{AV} = \mathbf{VB}$	$\mathbf{AX} = \mathbf{X}^*\mathbf{C}$
eigenvalue/eigenvector	**coneigenvalue/coneigenvector**
$\mathbf{A}\mathbf{v_k} = \lambda_k \mathbf{v_k}$	$\mathbf{A}\mathbf{x_k} = \xi_k \mathbf{x_k}^*$

A. On similarity and consimilarity equivalence relations of complex matrices:

A complex matrix $\mathbf{A} \in \mathbb{C}^{n\times n}$ may be characterized by two equivalence relations (similarity and conjugate similarity), defined as in Table II. The eigenvalue decomposition (left column, lower half, Table II) is a particular type of *similarity* transformation. In this case, $\mathbf{B}$ is diagonal with eigenvalues λ_k, $k \in [1, n]$ on its diagonal and the associated eigenvectors $\mathbf{v}_k$ as the columns of the transformation matrix $\mathbf{V}$. Also, if two matrices have the same n distinct eigenvalues, they are similar to the same diagonal matrix. There exists a family of matrices which are similar to one another and similar to the same diagonal form. However, in the case of (at least two) equal eigenvalues, it may not always be possible to have a diagonal form for a matrix and an almost-diagonal form, the Jordan form, may be used. According to Jordan's theorem [3], every square matrix $\mathbf{A}$ is similar to a Jordan matrix with Jordan blocks on the diagonal. A short summary of the Jordan blocks theory is contained in Appendix A-B.

The *conjugate similarity* equivalence (right column, Table II) is defined only for complex matrices, so matrix $\mathbf{A}$ may be brought to a diagonal (or, almost diagonal) form under consimilarity. For consimilarity diagonalization, $\mathbf{C}$ is diagonal, with ξ_k, $k \in [1, n]$ as coneigenvalues. In such case, the columns $\mathbf{x}_k$ of the transformation matrix $\mathbf{X}$ are all coneigenvectors and geometrically span orthogonal subspaces. This particular case of orthogonal consimilarity is always valid for $\mathbf{A}^T = \mathbf{A}$ (symmetric $\mathbf{A}$). However, in the general case, a diagonal form under consimilarity may not be always achieved (as we have discussed for similarity) and one has to consider an extended form of the transformation.

As already specified, with the radar scattering response typically represented using the so-called Backscatter Alignment (BSA) convention, the conjugate similarity operation appears for transformations involving a general scattering matrix, $\mathbf{S} \in \mathbb{C}^{2\times 2}$.

To the best of our knowledge, there are no direct mathematical formulations for solving a consimilarity transformation between two complex matrices. However, the generic methods which are present in the literature involve modifying the initial representation as to allow solving a similarity transformation between two equivalent forms of the initial complex matrices.
The earlier representation, studied extensively by Horn [3], [44] has involved performing the similarity relation between two power matrices: for example, if $(\mathbf{A}^H\mathbf{A})$ and $(\mathbf{C}^H\mathbf{C})$ are similar with nonnegative eigenvalues,

then $\mathbf{A}$ and $\mathbf{C}$ are conjugate similar. We recall that, in the domain of radar polarimetry, this method is based on the earlier model of unitary congruence introduced by Graves [45], known simply as the Graves method [46] [47]. Despite the justification that unitary congruence remains applicable only for a very particular case, namely for validation of reciprocity in monostatic measurements, the use of the Graves method remains employed for coneigenvalues/coneigenvectors calculation, as a general method.

The unitary consimilarity (also found as unitary congruence) has been extensively studied by Lüneburg, Cloude and Boerner [4], [46] for the reciprocal scattering matrix case. Moreover, they introduced the use of the SVD transformation for calculations involving bistatic/nonreciprocal matrices [6].

Starting from the concept of directional polarization vectors, originated by Graves [45], Lüneburg proposes, for monostatic radar polarimetry, to interpret the conjugate similarity transformation as a time reversal operation, i.e., an operation described by an antilinear operator. The antilinear operator connects then the conjugate propagation spaces for the transmitted and received electric fields, travelling in opposite directions. As part of this mathematical formalism, the Sinclair matrix becomes just the antimatrix, or the matrix of the antilinear operator [8]. Bebbington opposes this interpretation and proposes instead the use of the spinorial formalism in radar backscattering [48].

Preserving the formalism of the power matrix similarity, in the domain of mathematics, Ikramov introduces a more comprehensive definition of solving consimilarity [49] [50]. This formulation eliminated the special requirement of nonnegative eigenvalues, arguing that, alike simple eigenvalues, *"any matrix of order n has exactly n coneigenvalues (counting multiplicity)"* [50].

Moreover, other forms, containing block matrices and not the Hermitian semipositive power matrices, have been proposed for solving a consimilarity transformations. There are two main categories, differentiated by the constituent blocks of the equivalent matrices:

(a) A form with constituent blocks the original matrix and its complex conjugate [51] or transpose [52].
(b) A form with constituent blocks the real and imaginary parts of the original complex matrix [53] [54].

The equivalent form in (b) will be the one used in the current paper for a general scattering matrix. Ling et all. [55] have firstly proposed its utilization for the polarimetric scattering matrix. However, their original paper contained only a brief mathematical introduction of the concepts, lacking examples for practical applications of the theory. Moreover, from a theoretical aspect, it adopted closely the initial consimilarity definition of Hong and did not cover the particular case of complex eigenvalues of the real representation. In the current paper, we are going to address such shortcomings, and following the consimilarity definition from Ikramov, we are going to consider all possible cases.

B. Real representation of the scattering matrices:

We write the real representation block symmetric form of a scattering matrix (i.e., the RRSM), as:

$$\mathbf{S_{RR}} = \begin{bmatrix} \mathrm{Re}(\mathbf{S}) & \mathrm{Im}(\mathbf{S}) \\ \mathrm{Im}(\mathbf{S}) & -\mathrm{Re}(\mathbf{S}) \end{bmatrix} \tag{1}$$

$\mathbf{S_{RR}}$ is a 4×4 real matrix, for which we intend to find its diagonal form under similarity. For any real representation scattering matrix form, the eigenvalues decomposition has the property that all values will always be of the same mathematical type (Appendix B-C). This is due to the fact that the eigenvalues of any RRSM appear only in pairs: $\pm$ real pairs, or $\pm$ complex conjugate pairs. Because the RRSM has even dimensions, some matrices may have two real eigenvalues pairs (distinct or equal) while others will present only one $\pm$ complex conjugate set (hereafter also referenced as a "complex quad").

We already know that every square matrix is similar to a Jordan form with Jordan blocks on the diagonal. That is to say, for any RRSM, $\mathbf{S_{RR}} \in \mathbb{R}^{4\times4}$, we can find a similar matrix $\mathbf{B}$ of the same dimension as diagonal or upper/lower triangular Jordan form. If we recognize $\mathbf{B}$ to be just the RR form, $\mathbf{C_{RR}}$, of a complex matrix $\mathbf{C} \in \mathbb{C}^{2\times2}$, we have found a solution for the general consimilarity equation in Table II, upper-right corner. Due to the symmetry properties for the eigenvalues of $\mathbf{S_{RR}}$, in the general case, any matrix $\mathbf{B}$ can be written as the RR of a Jordan matrix.

We present the main steps for the implementation of the consimilarity transformation via the real representation in Algorithm I. In relation to the output matrices, the columns of $\mathbf{X}$ represent the coneigenvectors of the scattering matrix, while the diagonal elements/Jordan first order blocks from $\mathbf{C}$ will give the coneigenvalues.

For step (3), in the case of real, equal eigenvalues, two tolerance parameters with predefined values are used: δ_{imag} = 5% and $\delta_{r_{eq}} = 10^{-6}$. The first parameter is used to identify cases of real, equal eigenvalues coming

from initially classified complex values, but for which the imaginary part is considered negligible, i.e., smaller than the δ_{imag} times the real part. The second, $\delta_{r_{eq}}$, is a numerical tolerance under which the real eigenvalues are checked if equal.

C. Nonreciprocity factor and four particular types of complex matrices RRSMs:

We now introduce for our analysis the nonreciprocity factor (NRF), a complex parameter with values between $[-1, 1]$. This complex number has been presented in [56] for evaluating the degree of asymmetry of a scattering matrix:

$$\zeta = \frac{\sqrt{2}}{2}\frac{(S_{vh} - S_{hv})}{||\mathbf{S}||}. \tag{2}$$

, where $||\mathbf{S}|| = \sqrt{|S_{hh}|^2 + |S_{hv}|^2 + |S_{vh}|^2 + |S_{vv}|^2} = \sqrt{SPAN\,(\mathbf{S})}$

In [57], the authors use in their evaluation a nonreciprocity angle defined as the arctangent of the absolute value of the NRF, atan($|\zeta|$) $\in [0, \pi/4]$.
Other angular nonreciprocity parameters have been used in the literature: the Cameron nonreciprocity angle, θ_{rec} $\in [0, \pi/2]$ [58], or the difference in helicity parameters for the bistatic extended Target Scattering Vector Model (TSVM) theory, $\tau_2 = \tau_R - \tau_E \in [-\pi/2, \pi/2]$ [14].

With the current paper we use directly the nonreciprocity factor parameter. In Annex A-A, we show that the nonreciprocty factor can be rapidly expressed using only the elements of the Pauli vector.

In the followings, we evaluate the RRSM eigenvalues classification, along with the corresponding NRF, considering 4 particular types of complex matrices: complex symmetric, complex skew-symmetric, hermitian and skew-hermitian. While a scattering matrix may not exactly fit into one of these categories, it can nonetheless be expressed as a sum of such particular forms. For example, it is well-known that any complex square matrix can be decomposed into a sum of hermitian and skew-hermitian matrices.

We start our investigation from the general form in (3),

$$\mathbf{S} = \begin{bmatrix} a_1 + ia_2 & c_1 + ic_2 \\ d_1 + id_2 & b_1 + ib_2 \end{bmatrix} \tag{3}$$

with $a_1, a_2, b_1, b_2, c_1, c_2, d_1, d_2 \in \mathbb{R}$, from which we model the 4 particular examples of complex matrices. Due to text alignment constraints, we include at the end of the paper, in Table V, a summary representation of the

---

Algorithm I: Consimilarity solution via RRSM similarity transformation.
INPUT: Scattering matrix ($\mathbf{S}$)
OUTPUT: Transformation matrix ($\mathbf{X}$), Diagonal (or, general) form under consimilarity ($\mathbf{C}$)

1) Write scattering matrix $\mathbf{S}$ in RR form (eq. 1).
2) Extract eigenvalues (λ_k) and eigenvectors ($\mathbf{v}(\lambda_k)$) of $\mathbf{S_{RR}}$ (if repeated or complex eigenvalues, use the Jordan algorithm for extracting the vectors).
3) Check if eigenvalues are real or complex:
   (a) *all real eigenvalues:*
      (i) For *real, distinct eigenvalues*:
      $\mathbf{C_{RR}}$ = diag([λ_1, λ_2, $-\lambda_1$, $-\lambda_2$]).
      For *real, equal eigenvalues*:
      Verify if $\mathbf{C_{RR}}$ remains diagonal, or is written using Jordan blocks of second order (Appendix A-B): $\mathbf{C_{RR}} = \mathbf{J}_2(\lambda) \oplus \mathbf{J}_2(-\lambda)$. We observe $\mathbf{C_{RR}}$ to be the real representation form of matrix $\mathbf{C} = \mathbf{J}_2(\lambda)$.
      (ii) Verify/Order the vectors in the similarity transformation matrix to match the order of eigenvalues from $\mathbf{C_{RR}}$:
      $\mathbf{T} = [\mathbf{v}(\lambda_1), \mathbf{v}(\lambda_2), \mathbf{v}(-\lambda_1), \mathbf{v}(-\lambda_2)]$,
      $\lambda_1 \geq \lambda_2 \geq 0$.
   (b) *all complex eigenvalues:*
      (i) Write $\mathbf{C_{RR}}$ with the real Jordan blocks: $\mathbf{C_{RR}} = \mathbf{J}_{r1}(\lambda, \lambda^*) \oplus \mathbf{J}_{r1}(-\lambda, -\lambda^*)$. We observe $\mathbf{C_{RR}}$ to be the real representation form of matrix $\mathbf{C} = \mathbf{J}_{r1}(\lambda, \lambda^*)$.
      (ii) Build the real transformation matrix $\mathbf{T_{(d)}}$ by column-wise operations with real and imaginary parts of (eigen)vectors $\mathbf{v}(\lambda), \mathbf{v}(\lambda^*), \mathbf{v}(-\lambda), \mathbf{v}(-\lambda^*)$:

$$\mathbf{T}(:,1) = \frac{1}{2}\left[\mathrm{Re}\left(\mathbf{v}(\lambda)\right) + \mathrm{Re}\left(\mathbf{v}(\lambda^*)\right)\right];$$
$$\mathbf{T}(:,2) = \frac{1}{2}\left[\mathrm{Im}\left(\mathbf{v}(\lambda)\right) - \mathrm{Im}\left(\mathbf{v}(\lambda^*)\right)\right];$$
$$\mathbf{T}(:,3) = -\frac{1}{2}\left[\mathrm{Im}\left(\mathbf{v}(-\lambda)\right) - \mathrm{Im}\left(\mathbf{v}(-\lambda^*)\right)\right];$$
$$\mathbf{T}(:,4) = \frac{1}{2}\left[\mathrm{Re}\left(\mathbf{v}(-\lambda)\right) + \mathrm{Re}\left(\mathbf{v}(-\lambda^*)\right)\right];$$

4) Compute consimilarity transformation matrix $\mathbf{X}$ by using the relationship [53]:
   $\mathbf{X} = \frac{1}{4}[\mathbf{I_2}, i\mathbf{I_2}](\mathbf{T} - \mathbf{Q}_4\mathbf{T}\mathbf{Q}_4)[\mathbf{I_2}; i\mathbf{I_2}]$.
   where $\mathbf{I_2}$ represents the 2×2 identity matrix and $\mathbf{Q_4} = \begin{bmatrix} \mathbf{0} & -\mathbf{I_2} \\ \mathbf{I_2} & \mathbf{0} \end{bmatrix}$.
5) Verify compliance of consimilarity solution: $\mathbf{X}^{-1}\mathbf{S}\mathbf{X}^* = \mathbf{C}$

---

particular scattering matrices in each case, along with their real representation scattering matrices and Pauli scattering vectors.

(a) *complex symmetric,* $\mathbf{S} = \mathbf{S^T}$:
For a complex symmetric scattering matrix, its Pauli target vector may have non-zero elements for the first three components. It can be rapidly assessed that the RR of a reciprocal (symmetric) scattering matrix is itself symmetric, $\mathbf{S_{RR}} = \mathbf{S_{RR}^T}$. This matrix can be brought to a diagonal form through an eigen-decomposition and its four eigenvalues will all be real (in equal or distinct $\pm$ pairs). The NRF parameter has the value of 0.

(b) *complex skew-symmetric,* $\mathbf{S} = -\mathbf{S^T}$:
The Pauli decomposition of a skew-symmetric $\mathbf{S}$ is characterized alone by the asymmetric scattering mechanism (i.e., non-zero value on fourth row of Pauli target vector, Table V).
Here, both $\mathbf{S}$ and $\mathbf{S_{RR}}$ are skew-symmetric. The absolute value of NRF parameter for a skew-symmetric $\mathbf{S}$ is equal to 1. It is well known that for any skew-symmetric matrix with real entries, its eigenvalues are purely imaginary. For this reason, the eigenvalues of the RR will have the particular form of a double $\pm$ imaginary pair.

(c) *hermitian,* $\mathbf{S} = \mathbf{S^H}$:
The RR of a hermitian scattering matrix can be decomposed into both a real symmetric ($\mathbf{S_{RR_{c1}}}$) and a real skew-symmetric component ($\mathbf{S_{RR_{c2}}}$):

$$\mathbf{S_{RR}} = \mathbf{S_{RR_{c1}}} + \mathbf{S_{RR_{c2}}} \tag{4}$$
$$= \underbrace{\begin{bmatrix} a_1 & c_1 & 0 & 0 \\ c_1 & b_1 & 0 & 0 \\ 0 & 0 & -a_1 & -c_1 \\ 0 & 0 & -c_1 & -b_1 \end{bmatrix}}_{\mathbf{S_{RR_{c1}}}} + \underbrace{\begin{bmatrix} 0 & 0 & 0 & -c_2 \\ 0 & 0 & c_2 & 0 \\ 0 & -c_2 & 0 & 0 \\ c_2 & 0 & 0 & 0 \end{bmatrix}}_{\mathbf{S_{RR_{c2}}}}$$

$a_1, b_1, c_1, c_2 \neq 0$.

The NRF of a hermitian scattering matrix has the general form:

$$\zeta = \frac{i \cdot \sqrt{2} c_2}{\sqrt{(a_1)^2 + (b_1)^2 + 2({c_1}^2 - {c_2}^2)}} \tag{5}$$

The RRSM eigenvalues, of a hermitian matrix, can appear both in real pairs or as complex quad type. Matrices $\mathbf{H_1}$ and $\mathbf{H_2}$ are chosen for demonstrative purposes. They are both hermitian matrices, but while the eigen-analysis for the RR of $\mathbf{H_1}$ returns real and distinct $\pm$ eigenvalues pairs, the RR of $\mathbf{H_2}$ has only complex eigenvalues.

$$\mathbf{H_1} = \begin{bmatrix} 0.5431 & 0.498 - 0.0635i \\ 0.498 + 0.0635i & 0.1857 \end{bmatrix}$$

$$\mathbf{H_2} = \begin{bmatrix} 0.2673 & 0.1513 + 0.798i \\ 0.1513 - 0.798i & 0.0057 \end{bmatrix}$$

The absolute values of the nonreciprocify factor for H_1 and H_2 are 0.0984 and 0.9569, respectively.

(d) *skew-hermitian,* $\mathbf{S} = -\mathbf{S^H}$:
Here, we observe that the Pauli vector for a skew-hermitian matrix contains only imaginary elements (Table V). In terms of RR eigenvalues classification, because the RR of the skew-hermitian presents again both a symmetric and a skew-symmetric component (6), some matrices may have only real eigenvalues ($\pm$ real pairs) and some others only complex ones. We take as examples matrices $\mathbf{SKH_1}$ and $\mathbf{SKH_2}$, which return only real and only complex eigenvalues, respectively.

$$\mathbf{S_{RR}} = \mathbf{S_{RR_{d1}}} + \mathbf{S_{RR_{d2}}} \tag{6}$$
$$= \underbrace{\begin{bmatrix} 0 & 0 & a_2 & c_2 \\ 0 & 0 & c_2 & b_2 \\ a_2 & c_2 & 0 & 0 \\ c_2 & b_2 & 0 & 0 \end{bmatrix}}_{\mathbf{S_{RR_{d1}}}} + \underbrace{\begin{bmatrix} 0 & c_1 & 0 & 0 \\ -c_1 & 0 & 0 & 0 \\ 0 & 0 & 0 & -c_1 \\ 0 & 0 & c_1 & 0 \end{bmatrix}}_{\mathbf{S_{RR_{d2}}}}$$

$a_2, b_2, c_1, c_2 \neq 0$.

$$\mathbf{SKH_1} = \begin{bmatrix} 0.9963i & 0.6403 + 0.3043i \\ -0.6403 + 0.3043i & 0.39i \end{bmatrix}$$

$$\mathbf{SKH_2} = \begin{bmatrix} 0.958i & -0.7621 + 0.7211i \\ 0.7621 + 0.7211i & 0.2723i \end{bmatrix}$$

The NRF parameter of a general skew-hermitian matrix is:

$$\zeta = \frac{-\sqrt{2} c_1}{\sqrt{2{c_1}^2 - 2{c_2}^2 - {a_2}^2 - {b_2}^2}} \tag{7}$$

The nonreciprocify factor computed for SKH_1 and SKH_2 is -0.6176 and 0.6031, respectively. In this case, taking only the absolute value of the NRF, the matrices may be considered having similar properties. The RRSM eigenvalues classification is able to identify some distinct characteristics for the two.

With the current Section, we have introduced the definition of the RRSM in the process of solving the conjugate similarity equation. Our method combines definitions and properties from more recent mathematical papers offering a unique method that can be applied for any complex scattering matrix, reciprocal or not. Moreover, we have studied the connection with the NRF parameter and the classification of RRSM eigenvalues type, obtained in the intermediate step of decomposing $\mathbf{S_{RR}}$. With the additional information from NRF, we can improve the discrimination offered by the RRSM eigenvalues type. For example, while real eigenvalues solutions can be obtained from both reciprocal, hermitian or skew-hermitian scattering matrices, the value

of the NRF parameter can help discern between the three cases. Additionally, it was shown here that by increasing nonreciprocity of a scattering matrix (i.e., from a symmetric to a skew-symmetric value), the RRSM eigenvalues solutions can move from completely real to completely imaginary. In the experimental part, we want to see if this connection remains relevant when evaluated for scattered signals under increasing bistatic angles.
For scattering matrices which under Graves consimilarity decomposition returned non-orthogonal eigenvectors, E. Lüeneburg uses the term of inhomogeneous matrices. With the real representation scattering matrix, this corresponds primarily to some of the cases which present equal eigenvalues and only generalized eigenvectors (i.e., one double coneigenvalue and generalized coneigenvectors). However, there is one more case of inhomogeneous scattering matrices, not covered previously but presented in the current paper, during this chapter. We refer here to the case of RRSM presenting conjugate quad eigenvalues and which in turn, have one complex coneigenvalue pair and generalized coneigenvectors.

It is a common understanding that under bistatic observations, the reciprocity property of the polarimetric scattering matrices (with the BSA convention) is no longer valid. The examples from Section II, for both old and upcoming bistatic experiments have shown the strong interest of the recent years for civilian applications under bistatic geometries.

That is why, for the remaining of the paper, we concentrate our analysis on bistatic scattering mechanism characterization by using the real representation and its properties from the current section. The bistatic response of three elementary targets will be investigated through simulation. Two of our basic study methods will be the RRSM eigendecomposition classification and the scattering matrix NRF evaluation.

IV. Elementary scatterers under bistatic simulated observations

The radar cross-section (RCS) of targets with various shapes can be estimated with the help of computationally electromagnetic software. We intend to characterize the bistatic scattering response of three elementary targets ((a) dihedral, (b) square plate and (c) sphere) and resort to consider several incidence directions which will cover both small and large bistatic angles, $\beta \in [0^o, 90^o]$.

A. Bistatic Coordinate System Definition

In this subsection we introduce the schematic of a general bistatic geometry and estimate the bistatic angle between an incident and a scattering direction. The transmitting and receiving positions are specified in a spherical coordinate system (Fig. 2). We represent the scattering versors for the two possible conventions: $\hat{\mathbf{k}_{\mathbf{fs}}}$ (orange, for FSA) and $\hat{\mathbf{k}_{\mathbf{bs}}}$ (red, for BSA).

The angular pairs (θ_i, φ_i), (θ_s, φ_s) identify the incidence and scattering directions, with unit vectors $\hat{\mathbf{k}_{\mathbf{i}}}$ and $\hat{\mathbf{k}_{\mathbf{bs}}}$, respectively. For the monostatic case, the double equality for the angular parameters is obvious: $\theta_i = \theta_s$, $\varphi_i = \varphi_s$. The azimuth angles φ are defined in the XOY plane. The incident and scattered bistatic vectors determine the so-called bistatic plane of scattering [59], [60].

We consider the incidence versor:

$$\hat{\mathbf{k}_{\mathbf{i}}} = [-\cos\varphi_i \sin\theta_i, -\sin\varphi_i \sin\theta_i, -\cos\theta_i]^T$$

and, for a backscattering configuration, we have $\hat{\mathbf{k}_{\mathbf{i}}} = \hat{\mathbf{k}_{\mathbf{s}}}$ [61]. With a pair of incidence and scattering directions, the bistatic angle determined by the two is:

$$\beta = \cos^{-1}(\hat{\mathbf{k}_{\mathbf{i}}} \cdot \hat{\mathbf{k}_{\mathbf{s}}}) \tag{8}$$

As an example, Fig. 3 presents graphically the variation of bistatic angles in the scattering space with all angular combinations of $\varphi_s \in [-90^o, 90^o]$ and $\theta_s \in [-90^o, 90^o]$, for an arbitrarily selected incidence direction: $\{\theta_i = 30^o, \varphi_i = 0^o\}$. In this case, we observe a bistatic angle variation ranging between $0^o - 110^o$. A dotted grid delimiting the domain in iso-bistatic-angle regions, with a step variation of 10^o, is superimposed on the main figure.

B. Bistatic CST Simulations

Bistatic simulations have been performed using the CST Microwave Studio (CST MWS) software and its full-wave Time Domain and Integral Equation Solvers. The simulator is used for estimating the electric field responses for a given range of bistatic scattering directions. The polarimetric scattering matrix describes the relation between an incident ($\mathbf{E^i}$) and a scattered ($\mathbf{E^s}$) electric field. For measurements at a given frequency (wavelength, λ), bistatic range ($r_\beta = r_{Tx-Tg} + r_{Tg-Rx}$) and having linear horizontal (H) and vertical (V) bases, we can write:

$$\begin{bmatrix} E_H^s \\ E_V^s \end{bmatrix} = \frac{e^{-j\frac{2\pi}{\lambda \cdot r_\beta}}}{\sqrt{r_{Tx-Tg} \cdot r_{Tg-Rx}}} \begin{bmatrix} S_{hh} & S_{hv} \\ S_{vh} & S_{vv} \end{bmatrix} \cdot \begin{bmatrix} E_H^i \\ E_V^i \end{bmatrix} \tag{9}$$

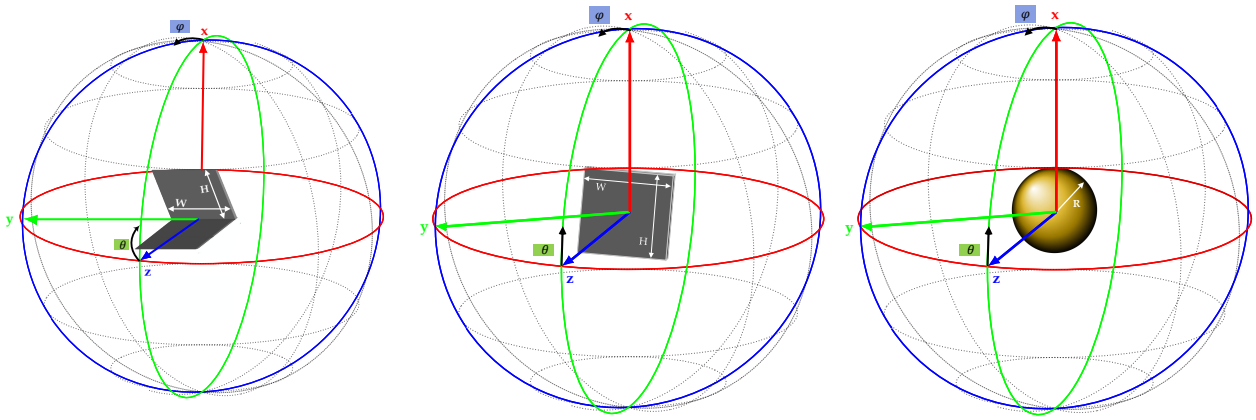

(a) (b) (c)

Fig. 1
Simulated scatterers in a spherical geometry representation: (a) Square plate. (b) Dihedral. (c) Sphere.

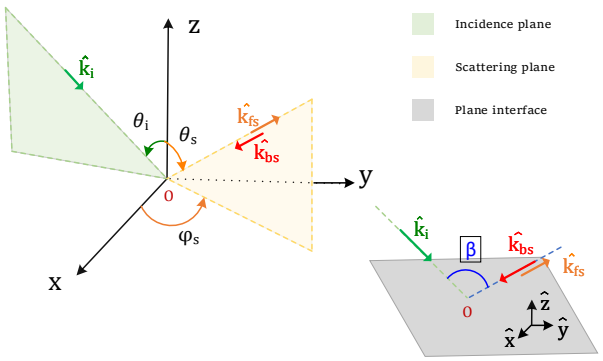

Fig. 2
Bistatic scattering geometry.

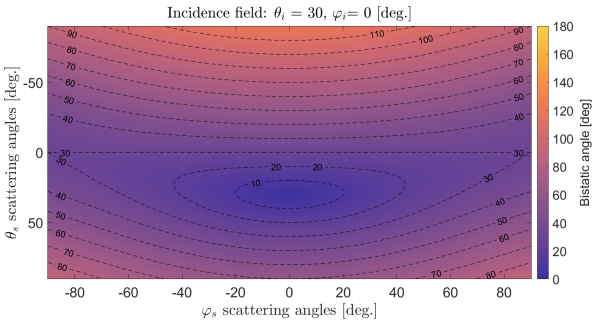

Fig. 3
Bistatic angles mapping with respect to scattering directions $\varphi_s, \theta_s \in [-90^o, 90^o]$, given the incidence directions $\varphi_i = 0^o$, $\theta_i = 30^o$.

Without the phase change propagation term of (9) and for known values of the incidence field components, E^i_H and E^i_V, the elements of the scattering matrix can be estimated from the scattered field. The vertical and horizontal components of the incidence polarization vector are of unit value, equal to 1 V/m at each incidence. A spherical coordinate system is used to describe and compute the numerically simulated fields. For every simulated incidence combinations, we have the angle $\varphi_i = 0^o$ fixed, while we modify angle θ_i. We choose to represent the results for all bistatic scattering directions between $\theta_s, \varphi_s \in [-45^o, 45^o]$ (0.5^o step) and three incidence directions: (θ_i, φ_i)= $\{(0^o, 0^o), (25^o, 0^o), (40^o, 0^o)\}$. The bistatic angle ($\beta$) will takes values from $[0^o, 90^o]$.

The geometry of the three elementary targets and their orientation with respect to the coordinate system is modelled in Fig. 1. Each target is located with their

TABLE III
Percentages for each class of the RRSM eigenvalues type classification (responses in the (θ_s, φ_s) scattering space) for the three analysed targets (90^o dihedral, square plate, sphere). We consider the incidence directions (θ_i, φ_i) of $\{(0^o, 0^o), (25^o, 0^o), (40^o, 0^o)\}$.

Incidence direction (θ_i, φ_i)	Real eigvs. pairs [%] **distinct**	**equal**	Complex eigvs. pairs [%]	Total [%]
90^o Dihedral				
$(0^o, 0^o)$	62.23	30.86	6.9	100
$(25^o, 0^o)$	73.17	7.17	19.65	100
$(40^o, 0^o)$	63.91	2.28	33.81	100
Square Plate				
$(0^o, 0^o)$	14.25	1.21	84.54	100
$(25^o, 0^o)$	21.95	1.81	76.24	100
$(40^o, 0^o)$	30.46	3.2	66.34	100
Sphere				
$(0^o, 0^o)$	4.62	1.46	93.92	100
$(25^o, 0^o)$	4.94	1.54	93.52	100
$(40^o, 0^o)$	4.57	1.95	93.48	100

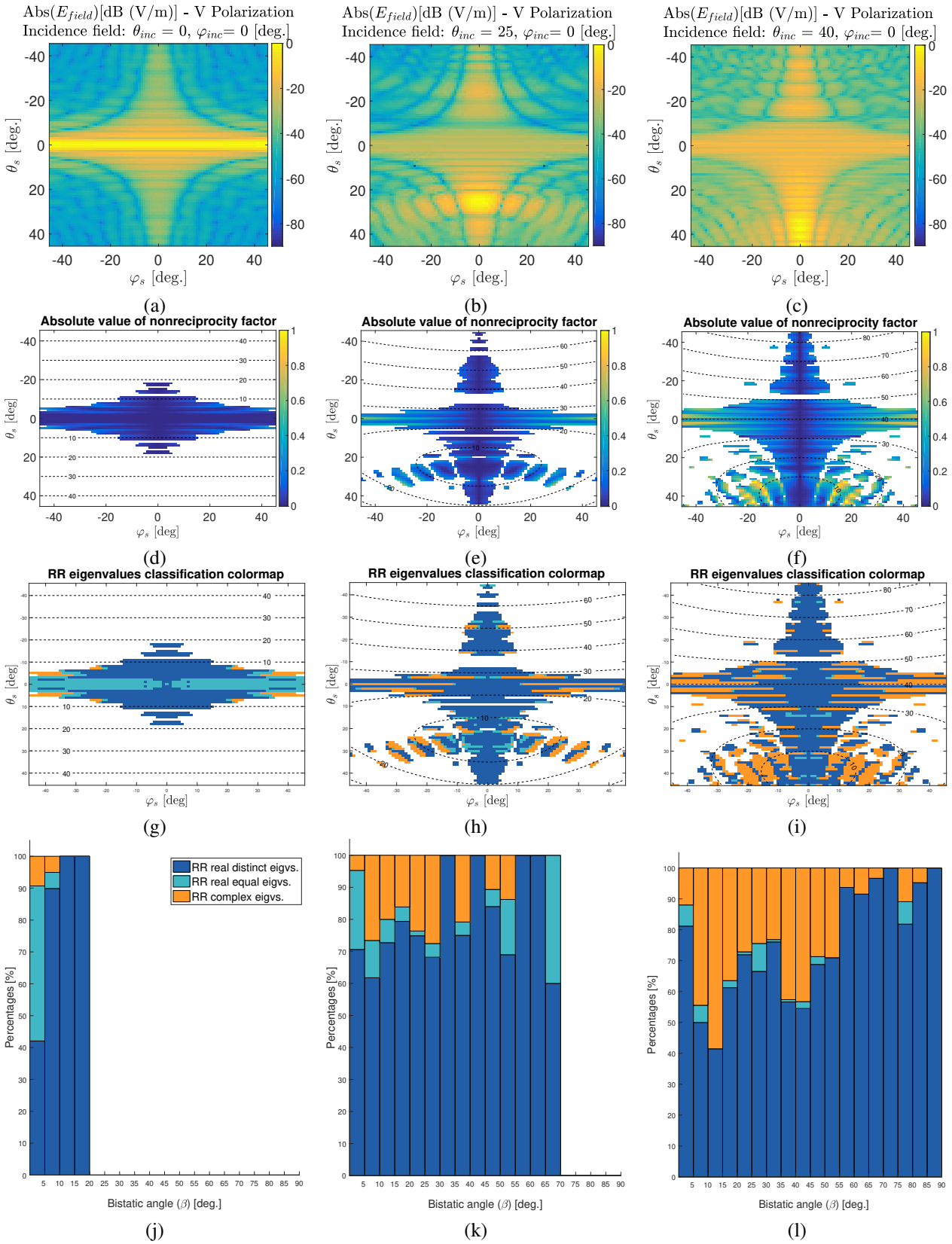

Fig. 4

90^o Dihedral (Time Domain Solver Results). Incidence directions at $\varphi_i = 0^o$ and $\theta_i = 0^o$ (first column), $\theta_i = 25^o$ (second column), $\theta_i = 40^o$ (third column) and scattering directions $\theta_s, \varphi_s \in [-45^o, 45^o]$. (a)-(c) Normalized absolute value of scattered bistatic E_{field} in V Polarisation. (Following results are after selecting scattering directions at which Abs(E_{field}) $\geq$ -30 dB) (d)-(f) Absolute values of nonreciprocity factor. (g)-(i) RRSM colormap of eigenvalues classification type. (j)-(l) RRSM eigenvalues classification type for bistatic angle intervals between $[0^o, 90^o]$.

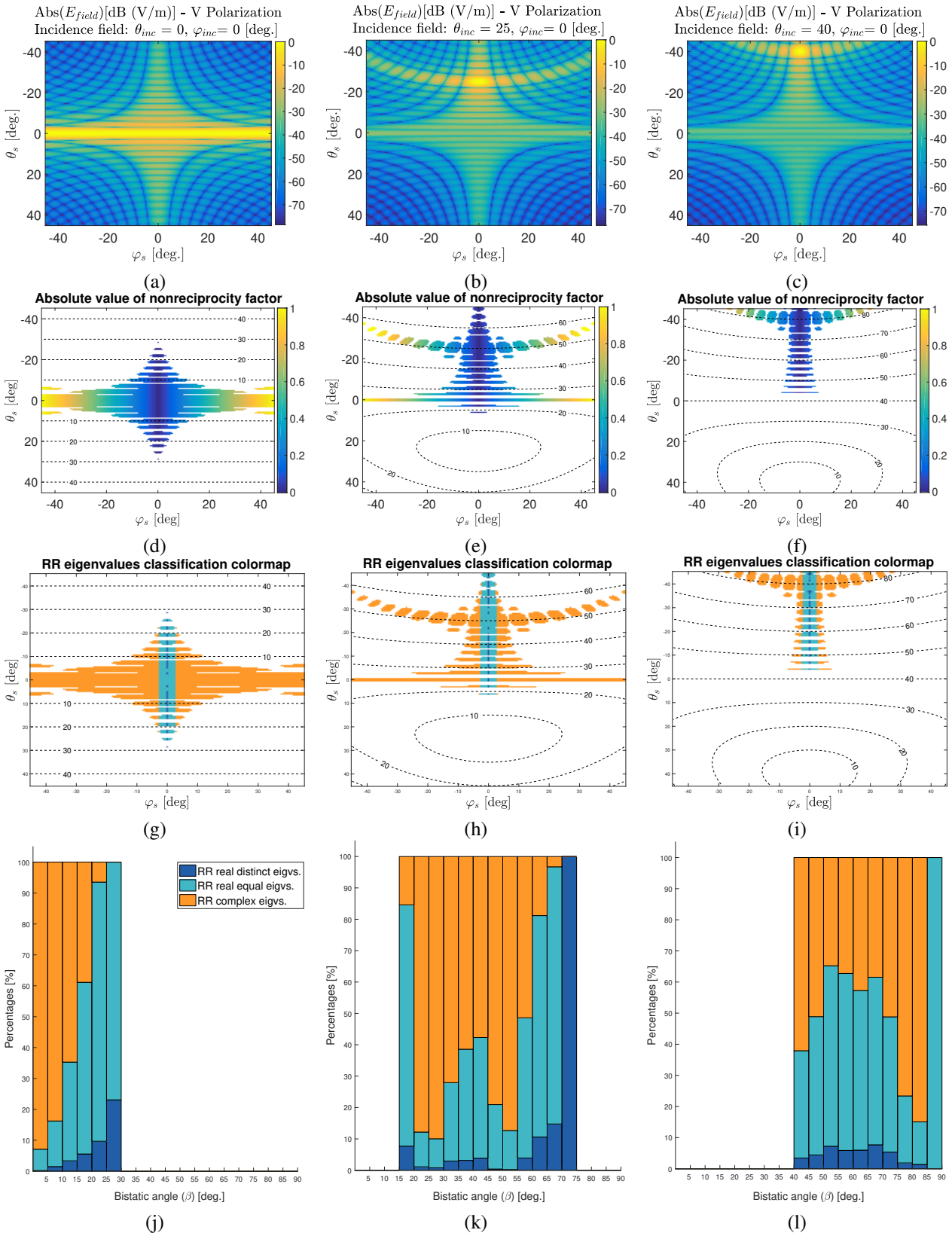

Fig. 5
Square Plate (Time Domain Solver Results). Incidence directions at $\varphi_i = 0^o$ and $\theta_i = 0^o$ (first column), $\theta_i = 25^o$ (second column), $\theta_i = 40^o$ (third column) and scattering directions $\theta_s, \varphi_s \in [-45^o, 45^o]$. (a)-(c) Normalized absolute value of scattered bistatic E_{field} in V Polarisation. (Following results are after selecting scattering directions at which Abs(E_{field}) $\geq$ -30 dB) (d)-(f) Absolute values of nonreciprocity factor. (g)-(i) RRSM colormap of eigenvalues classification type. (j)-(l) RRSM eigenvalues classification type for bistatic angle intervals between $[0^o, 90^o]$.

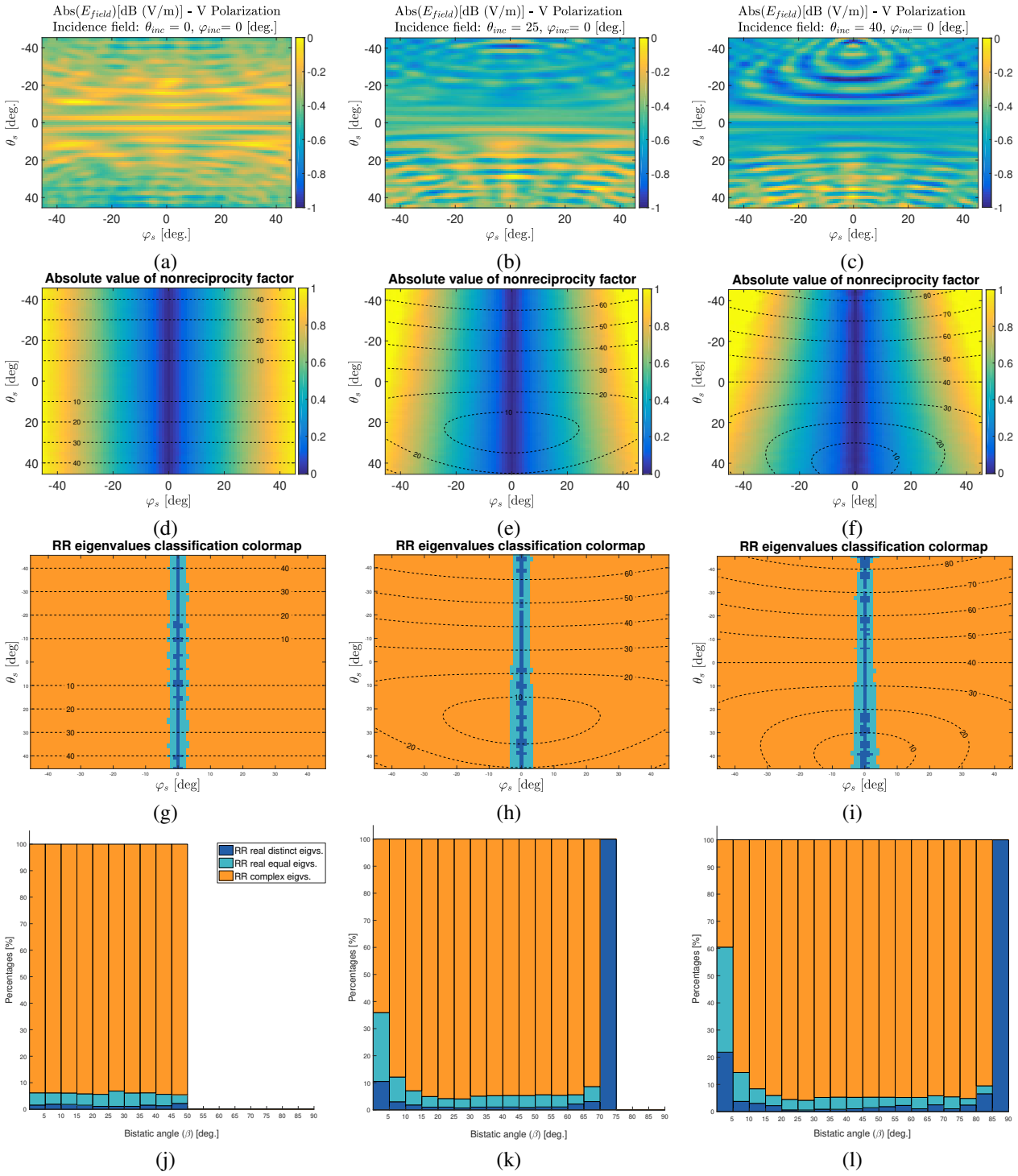

Fig. 6
Sphere R=16λ (Integral Equation Solver Results). Incidence directions at $\varphi_i = 0^o$ and $\theta_i = 0^o$ (first column), $\theta_i = 25^o$ (second column), $\theta_i = 40^o$ (third column) and scattering directions $\theta_s, \varphi_s \in [-45^o, 45^o]$. (a)-(c) Normalized absolute value of scattered bistatic E_{field} in V Polarisation. (d)-(f) Absolute values of nonreciprocity factor. (g)-(i) RRSM colormap of eigenvalues classification type. (j)-(l) RRSM eigenvalues classification type for bistatic angle intervals between $[0^o, 90^o]$.

centre point in the origin and the incoming wave propagates from the positive Z direction towards origin. The variation of the φ angle is in the XOY plane (determined by the blue circle) and the variation of the θ angle is in the ZOX plane (green circle).

The simulations are performed for a C-Band central frequency, f=5.405 GHz and the three scatterers are shaped from PEC (Perfectly Electrical Conductor) material. They present large dimensions compared to the wavelength: a) right angle dihedral with square faces (i.e., equal height (H) and width (W)), H=W=16λ, b) square plate, H=W=20λ, and c) sphere of radius R = 16λ.

The CST simulator is used only for determining the scattered electric field values for all $\{\varphi_s, \theta_s\}$ combinations in the scattering space, while further post-processing is performed with the MATLAB software.

C. 90^o Dihedral

For the dihedral target, limiting the extreme values of the angular scattering domain ($\theta_s, \varphi_s \leq 45^o$) ensures that we record responses only for scattering in the interior of the dihedral (and possible edge diffraction only for near marginal positions, $\theta_i, \varphi_i = 40^o \div 45^o$). In Fig. 2, the joint edge of the dihedral is oriented along the Y axis (with the centre point of the edge corresponding to the origin of the coordinate system) and the Z axis matches the direction of the dihedral's bisector.

The several subfigures shown in Fig. 4 help us in characterizing the dihedral response (the same type of subfigures will be used also for the other two scatterers). On the first row, the simulated normalized absolute electric field values (V Polarization) are displayed. For figures on rows 2-4, we limit our observations only to those directions for which the normalized electric field is larger than -30 dB. The shape of our selection and the number of points fulfilling such constraint modifies with the change in incidence direction (i.e., in our example, from one column to the other). Moreover, the figures in rows 2-3 are shown having an overlay with the iso-bistatic-angles grid, allowing us to investigate our parameters and their changes in direct link to the increase/decrease of the bistatic angle. The second row reveals the modulus of the NRF parameter for the scattering matrices estimated, at each position in the scattering space, based on the simulated electric field values. The third row contains a colormap representation of the RRSM eigenvalues classification, with three main classes, as follows: orange - complex eigenvalues, dark blue - two real, distinct pairs of eigenvalues, cyan - two real, equal pairs of eigenvalues. In addition to this colormap, the percentage distribution, column-wise, for each incidence case, can be found in Table III. The RRSM eigenvalues classification as a function of the bistatic angle, displayed with 5^o increment, is shown on the fourth row. For each bistatic interval, the result is displayed in an absolute percentage scale (100% for summation of all three categories). The exact percentages can be consulted in Table VI. One can also determine the exact relative quotients for each category and each bistatic interval; in a relative scale analysis, all percentages of one category from Table VI should sum to the value in Table III.

At normal incidence scattering direction ($\theta_i = 0^o, \varphi_i = 0^o$), the absolute value of the nonreciprocity factor is quite low (Fig. 4d), $|NRF| \in [0, 0.3]$ and the eigen-classification performed on the RRSMs contains predominantly real eigenvalues (Fig. 4g). For our dihedral example, with more skewed incidence directions ($\theta_i = 25^o$ or 40^o), we observe an increase in the percentage associated to bistatic scattering directions returning complex eigenvalues results. Such increase is shown to appear generally at scattering directions with $|\varphi_s| > 5^o$, distributed in the entire range of θ_s values (Fig. 4h-i).

D. Square Plate

For the square plate scatterer, its dimensions are H = W = 20λ. This offers a form factor (FF, i.e., ratio of height to width) equal to one. As in the case of orthogonal dihedral, the Time Domain Solver of the computational program has been used for producing the electric field scattering responses. The main post-processing results are shown in Fig. 5d-l. The display of parameters in subfigures and their relation with results from Table III or Table VI remain the same as presented previously, in the dihedral subsection.

For the RRSMs eigenvalues classification, we observe from Table III and Fig. 5g-l a dominance of eigenvalues of complex quad type (all incidence alignments), when scattering angular parameter φ_s is outside $[-5^o, 5^o]$ and ($\forall$) θ_s.

E. Sphere

The sphere's bistatic response has been computed using the Integral Equation Solver (Frequency Domain analysis mode).

Firstly, we highlight the large amplitude response of the sphere compared to the (normalized) bistatic response

of the other two scatterers (in Fig. 6a-c, the computed electric field is larger than -3 dB for all observed scattering directions).

The RRSM eigenvalues classification is dominated by complex eigenvalues results (Fig. 6j-l) for angular directions φ_s outside a [-5^o, 5^o] interval. However, the change of the NRF absolute values is a gradual one (Fig. 6d-f) and only around $\varphi_s > 25^o$ the absolute values are larger than 0.5 . In this case, it appears that the complex eigenvalues of the RRSM appear even when having NRF modules of only 0.1-0.2 . A similar observation can be formulated for the plate's example. Moreover, common to all scatterers, we observe that for extreme values of bistatic angles in our incidence - scattering combinations, the RRSM eigenvalues are (predominantly) of real type.

For our three scatterers, we represent in Fig. 7, the amplitude of their complex RRSM eigenvalues (same for all values in a quad set) as a function of the bistatic angle and the NRF modulus. Even with different numbers of scattering points and distinct ranges for the absolute values, in each case, we observe a common pattern among the three graphs: when varying from incidence angle $\theta_i = 0^o$ (orange dots) to incidence angle $\theta_i = 40^o$ (pale pink dots), the amplitudes of the returned complex eigenvalues decrease globally; the same observation remains true if evaluating with respect to the bistatic angle. For the sphere scatterer, we observe a small dynamic range for the moduli of the complex RRSM eigenvalues. With the dihedral and sphere scatterers, the absolute value of the NRF can be anywhere inside the definition range, at all bistatic angles, while in the case of the plate's response, the NRF absolute values increase only for bistatic angles equal to integer multiples of θ_i. While we observe no complex eigenvalues results for NRF absolute values smaller than 0.05, this arrangement is also a direct consequence of implementing the threshold value δ_{imag} into our numerical evaluation workflow.

Analysing the variation of the complex absolute values other 3D visualization combinations (e.x., amplitude vs. bistatic angle vs. phase of NRF parameter or amplitude vs. NRF absolute value vs. phase of NRF), no other common patterns were identified.

V. General Remarks and Conclusions

In the previous section, we have simulated the bistatic scattering response (geometrical regime) of three elementary PEC targets. We summarize the main results, as follows.

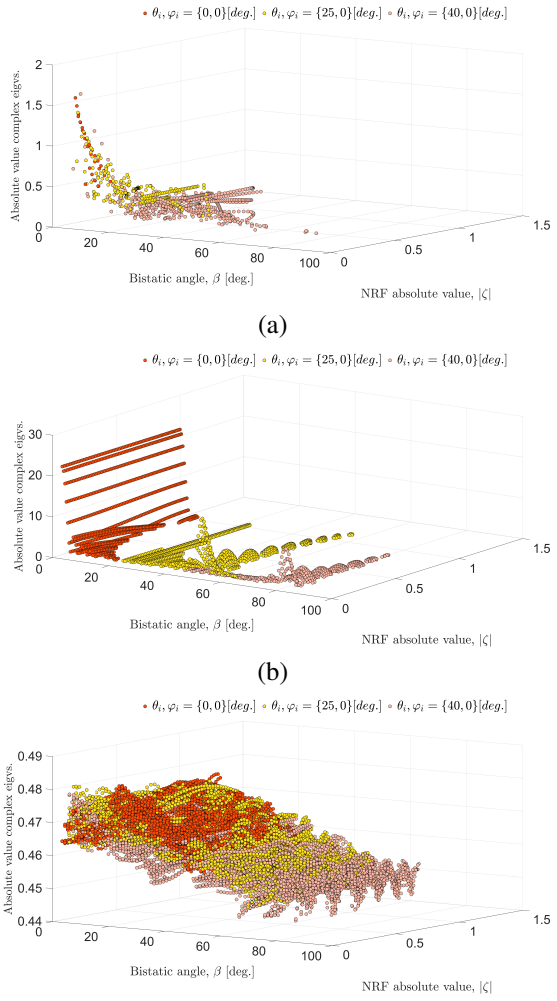

Fig. 7
Absolute value of all RRSM complex eigenvalues vs. bistatic angle vs. absolute value of the nonreciprocity factor, for all our three targets: (a) 90^o Dihedral (b) Square Plate (c) Sphere.

For the 90^o dihedral, by changing the θ_i observation angle to a more skewed incidence direction, we have observed an increase in the percentage of complex eigenvalues of the RRSMs decomposition. Also, the results seem in accordance with the assumption that the greater the deviation from monostatic normal incidence, the larger will be the computed NRF modulus and this will be reflected in an increased change of RRSM eigenvalues from real to complex (Fig. 4 g-i and j-l).

On the other hand, the eigenvalues type percentages of the sphere's response (complex dominated) remained almost invariant to the changes in the incidence direction. Here, the absolute values of the NRF were not any longer a relevant indicator on their own, for the

RRSM eigenvalues type. In case of the square plate, the percentages of RRSMs eigenvalues distribution appeared to have a different tendency: some statistical variations resulting in the decrease of the percentage of RRSM complex eigenvalues, while increasing θ_i, were shown (Table III). Another particular trend was the appearance of local peaks of the RRSM complex eigenvalues classification for integer multiples of the θ_i, when evaluated in relation to the bistatic angles. The results obtained here, appear to be in accordance with the observation of [61], where it is argued that for the general radar scattering geometry, nonsymmetric scattering matrix responses may appear even for symmetric targets. Results from other publications, for example in [62] (which presents in-facility conducted experiments), confirm that the bistatic response of metallic plates/disks are greatly alignment-sensitive.

Relating monostatic and bistatic measurements is an old interest of polarimetric studies. Around 1965, Kell formulated a first monostatic to bistatic equivalence theorem (MBET) [63]. A review for some of the well-known MBET formulations is given in the introduction of [64]. Generally, it is acknowledged in the radar community that under given conditions, the bistatic RCS is equal to the monostatic RCS measured on the bisector of the bistatic angle. In [65], authors have made and attempt for determining threshold values for the compliance of the MBET for 2D scatterers simulated results. It has been shown that the MBET depends greatly on the so-called "smoothness" of a point target (a property characterizing the ability of a target to produce single or multipath propagating phenomenons) and the angular interval for MBET compliance decreases for targets having a geometry which produces multipath and shadowing effects. In their study, for the experimental target characterized as having the "smoothest" response, the estimated angle for which the MBET RCS equivalence holds was $\approx 14^o$, while for their most complex shaped object, the compliance was for only $\approx 1.5^o$ misalignment.

With our simulations, for all three simple shaped elementary scatterers, we have observed a total interval of $\approx 10^o$ degrees (left-right variation in the φ scattering direction) in which the RRSM eigenvalues are of real type, for all considered incidence directions. As discussed in the theoretical section, such result is true for both symmetric and hermitian/skew-hermitian bistatic matrices having zero or very low NRF moduli values, respectively. Here, having $\varphi = 0^o$, we consider the case to be that of symmetric/almost symmetric scattering matrices. In this context, the presence of RRSM real eigenvalues can suggest the angular interval for which the reciprocity property of the scatterers is conserved, and this observation, for the three PEC targets, appears to be in accordance to the MBET values proposed by experimental evaluations for the case of "smooth" targets.

In the current paper, the real representation scattering matrix (and particularly the RRSM eigenvalues investigation) has proven as a valuable tool for offering new information of general scattering matrices evaluated under bistatic geometries. Introducing a complete RRSM theory for evaluating general scattering matrices under consimilarity is one of the paper's main contributions. The bistatic simulations of the targets, performed under the computational electromagnetic program, have served as support for our polarimetric analysis.

Some of our results from Fig. 7 have revealed that there are positions presenting complex RRSM eigenvalues and having also quite small values of their NRF moduli (which would normally be associated with a small nonreciprocity degree). We argue that the relationship between the type of eigenvalues and the NRF parameter appears to be a more complex one for bistatic observations and other parameters, as the bistatic angle, should always be taken into account. With future studies, we intend to better characterize this dependence, identify connections to real scattering properties, expand the applicability of the real representation scattering matrix description and also study new relevant parameters for evaluation in the bistatic polarimetric domain.

APPENDIX A

A. The Pauli Decomposition

A well known summation coherent decomposition is the Pauli decomposition [2] of the scattering matrix, $\mathbf{S}$:

$$\mathbf{S} = \begin{bmatrix} S_{hh} & S_{hv} \\ S_{vh} & S_{vv} \end{bmatrix} \tag{10}$$

$$= \frac{1}{\sqrt{2}} \left(k_0 \cdot \sigma_{\mathbf{0}} + k_1 \cdot \sigma_{\mathbf{1}} + k_2 \cdot \sigma_{\mathbf{2}} + k_3 \cdot \sigma_{\mathbf{3}} \right) \tag{11}$$

The basis matrices are:

$$\sigma_{\mathbf{0}} = \begin{bmatrix} 1 & 0 \\ 0 & 1 \end{bmatrix} \qquad \sigma_{\mathbf{1}} = \begin{bmatrix} 1 & 0 \\ 0 & -1 \end{bmatrix}$$

$$\sigma_{\mathbf{2}} = \begin{bmatrix} 0 & 1 \\ 1 & 0 \end{bmatrix} \qquad \sigma_{\mathbf{3}} = \begin{bmatrix} 0 & -i \\ i & 0 \end{bmatrix}$$

Coefficients k_0, k_1, k_2 and k_3 are, in general, complex numbers and (in the monostatic case), they are associated

to odd bounce, even bounce, diffuse scattering and the asymmetric scattering mechanism, respectively.

$$k_0 = \frac{S_{hh}+S_{vv}}{\sqrt{2}} \qquad k_1 = \frac{S_{hh}-S_{vv}}{\sqrt{2}}$$
$$k_2 = \frac{S_{hv}+S_{vh}}{\sqrt{2}} \qquad k_3 = \frac{i\,(S_{hv}-S_{vh})}{\sqrt{2}}$$

These values are grouped together in the form of the Pauli vector, $\mathbf{k} = [k_0, k_1, k_2, k_3]^T$. As usual, $i^2 = -1$.

Below, we express the NRF parameter used in the paper by means of Pauli vector ($\mathbf{k}$) elements:

$$\zeta = \frac{1}{\sqrt{2}} \frac{(S_{vh}-S_{hv})}{\sqrt{|S_{hh}|^2+|S_{hv}|^2+|S_{vh}|^2+|S_{vv}|^2}} = \frac{i \cdot k_3}{\sqrt{{k_0}^2+{k_1}^2+{k_2}^2-{k_3}^2}} \tag{12}$$

B. Jordan blocks general form

A Jordan matrix J is a direct sum (here, symbol $\oplus$) of Jordan blocks.

$$\mathbf{J} = \mathbf{J}_{p1} \oplus \mathbf{J}_{p2} \oplus \ldots \tag{13}$$

A Jordan block, $\mathbf{J}_p(\lambda_k)$, associated to an eigenvalue λ_k has dimensions $p \times p$. Every diagonal entry is equal to λ_k and there are also $p-1$ values of ones in the first upper-diagonal (or first lower-diagonal, depending on the convention), with the rest of the elements equal to zero.

$$\mathbf{J}_p(\lambda_k) = \lambda_k \mathbf{I}_p + \mathbf{L}_p \tag{14}$$

$$\mathbf{L}_p = \begin{bmatrix} 0 & 1 & \cdots & \cdots & 0 \\ 0 & 0 & \ddots & & \vdots \\ \vdots & \ddots & \ddots & \ddots & \vdots \\ \vdots & & \ddots & 0 & 1 \\ 0 & \cdots & \cdots & 0 & 0 \end{bmatrix}$$

As a quick example, the Jordan blocks of sizes 1, 2, 3 (for a real-value eigenvalue λ) are:

$$\mathbf{J}_1(\lambda) = \lambda \quad \mathbf{J}_2(\lambda) = \begin{bmatrix} \lambda & 1 \\ 0 & \lambda \end{bmatrix} \quad \mathbf{J}_3(\lambda) = \begin{bmatrix} \lambda & 1 & 0 \\ 0 & \lambda & 1 \\ 0 & 0 & \lambda \end{bmatrix}$$

When working with Jordan blocks of order larger than 1, the individual columns of the transformation matrix (associated to that block) are no longer all eigenvectors; there will be one eigenvector and $p-1$ generalized eigenvectors [66].

A real $n \times n$ matrix will have in general real and complex eigenvalues, the latter occurring in complex conjugate pairs. With complex eigenvalues, it is possible to have also complex (generalized) eigenvectors.

The Real Jordan form (R-Jordan) offers an equivalent of the canonical form but with real entries. The general idea behind creating a real Jordan block representation is based on combining the information offered by the real and imaginary parts of two complex conjugate eigenvalues and their corresponding eigenvectors (generalized eigenvectors, if the case). Consider a complex non-degenerate eigenvalue $\lambda = a + i \cdot b$, $a, b \in \mathbb{R}$. The pair (λ, λ^*) will have associated a square block of the form $\mathbf{J}_{r_1}$.

The real Jordan blocks of sizes 1, 2 are:

$$\mathbf{J}_{r_1}(\lambda, \lambda^*) = \begin{bmatrix} a & b \\ -b & a \end{bmatrix} = a\mathbf{I}_2 + b\mathbf{Q}_2^T, (\mathbf{Q}_2)^2 = -\mathbf{I}_2$$
$$\mathbf{J}_{r_2}(\lambda, \lambda^*) = \begin{bmatrix} \mathbf{J}_{r_1}(\lambda, \lambda^*) & \mathbf{I}_2 \\ \mathbf{0} & \mathbf{J}_{r_1}(\lambda, \lambda^*) \end{bmatrix}$$

The reader may encounter other resources in which the transpose of $\mathbf{J}_{r_1}$ from here is used as constructive block of the R-Jordan form.

APPENDIX B

A. Graves Matrix

The Graves matrix is a 2×2 Hermitian positive semidefinite matrix:

$$\mathbf{G} = \mathbf{S}^H \cdot \mathbf{S} = \begin{bmatrix} |S_{hh}|^2+|S_{vh}|^2 & S_{hh}\cdot S_{hv}^* + S_{vh}\cdot S_{vv}^* \\ S_{hv}\cdot S_{hh}^* + S_{vv}\cdot S_{vh}^* & |S_{vv}|^2+|S_{hv}|^2 \end{bmatrix} \tag{15}$$

Considering the type of eigenvalues returned by diagonalizing the Graves matrix, Lüneburg proposes to classify the scattering matrices as homogeneous or inhomogeneous [67]. On one hand, the homogeneous delimitation was used to separate the case of mathematically symmetric matrices, i.e., matrices which can be diagonalized by unitary consimilarity and thus have two orthogonal coneigenvectors. This type of algebraic operation is in some cases known as the Autonne-Takagi factorization. With symmetric matrices, the eigenvalues of $\mathbf{G}$ are the squared absolute values of the corresponding coneigenvalues [67]. On the other hand, according to Lüneburg, the case of inhomogeneous Sinclair matrices contains all scattering matrices for which their coneigenvectors are no longer orthogonal, but the eigendecomposition of the Graves matrix still returns real, non-negative values. Finally, the small percentage of matrices, for which the

TABLE IV
Observations with respect to eigenvalues of RRSM and the eigenvalues/eigenvectors of a SM.

Real Representation Scattering Matrix (RRSM)		**Scattering matrix (SM)**	
eigenvalues		conjugate eigenvalues	conjugate eigenvectors
real eigenvalues	**distinct** real pairs $\{\lambda_1, \lambda_2, -\lambda_1, -\lambda_2\}$	distinct real $\{\xi_1, \xi_2\}$	independent, orthogonal
	equal real pairs $\{\ \lambda, \lambda, -\lambda, -\lambda\ \}$	equal real $\{\ \xi, \xi\ \}$	a. independent, orthogonal or b. one coneigenvector and one generalized coneigenvector
complex eigenvalues	complex conjugate pairs $\{\lambda, -\lambda, \lambda^*, -\lambda^*\}$	complex ξ	one coneigenvector and one generalized coneigenvector

Graves matrix eigendecomposition returns no longer real positive values, are left outside this second case, because in the algebraic definition used by Lüneburg (originated in the work of Horn), such matrices do not present coneigenvalues and coneigenvectors [46].

B. Singular Value Decomposition

Under the Singular Value Decomposition, we write a complex matrix $\mathbf{S}$, as:

$$\mathbf{S} = \mathbf{U}\mathbf{\Sigma}\mathbf{V}^H \tag{16}$$

$\mathbf{\Sigma}$ is a non-zero matrix having only diagonal elements, arranged in a descending manner, and which are known as the singular values of $\mathbf{S}$. The singular values are non-negative real numbers. Matrices $\mathbf{U}$ and $\mathbf{V}$ are complex unitary: $\mathbf{U}^H\mathbf{U} = \mathbf{U}\mathbf{U}^H = \mathbf{I}$ and $\mathbf{V}^H\mathbf{V} = \mathbf{V}\mathbf{V}^H = \mathbf{I}$.

Extending the Graves definition from eq. 15 to that of the SVD expression, we have:

$$\mathbf{G} = \mathbf{V}\mathbf{\Sigma}^H\mathbf{U}^H\mathbf{U}\mathbf{\Sigma}\mathbf{V}^H = \mathbf{V}\mathbf{\Sigma}^H\mathbf{\Sigma}\mathbf{V}^H = \mathbf{V}\mathbf{G}_{\mathbf{\Sigma}}\mathbf{V}^{-1} \tag{17}$$

Matrix $\mathbf{G}_{\mathbf{\Sigma}}$ contains the eigenvalues of $\mathbf{G}$, which are no others than the squared singular values. Based on the observation from Appendix B-A, we conclude that for the case of symmetric matrices, the singular values of $\mathbf{S}$ are no different than the absolute values of the coneigenvalues. While for asymmetric scattering matrices, the coneigenvalue remark does not verify any more, it remains true that a squared relation exists between the eigenvalues of the Graves matrix and the singular values of $\mathbf{S}$. It is therefore possible to compute one from the other (while ignoring for some cases a potential sign difference, i.e., a phase ambiguity).

C. Eigenvalues of the real representation scattering matrix (RRSM)

Starting from the definition of the RRSM in eq. (1), we have $\mathbf{S}_{\mathbf{RR}} \in \mathbb{R}^{4\times4}$, which is twice the dimension of the initial scattering matrix, $\mathbf{S} \in \mathbb{C}^{2\times2}$.

As a general property, of the proposed real representation matrix, its eigenvalues can always be found in positive-negative pairs. Due to the particularity of this mapping, we present in Table IV, the immediate connection between the parameters (coneigenvalues/ eigenvalues) obtained from decomposing one general scattering matrix and its real representation form, respectively. Any real pair of eigenvalues $(\lambda_k, -\lambda_k)$, $k = 1, 2$, has associated exactly one positive real coneigenvalue, $\xi_k = \lambda_k$, $\lambda_k > 0$. The eigenvectors set corresponding to the RRSM eigenvalues pair will be used in computing the con(jugate) eigenvector of ξ_k (as in Algorithm I).

For the case of complex eigenvalues of $\mathbf{S}_{\mathbf{RR}}$, the coneigenvectors of $\mathbf{S}$ will no longer be orthogonal. We obtain, one coneigenvector and one generalized coneigenvector. This can also appear if the eigenvalues computed from RRSM are equal and their eigenvectors are no longer independent.

APPENDIX C
EXTRA TABLES

Two tables have been excluded from the main text and can be found hereafter. The reader can discover in Table V the distinctive forms of the scattering matrix, the Pauli vector and the real representation forms of the 4 types of matrices analysed in detail in Section III.
With respect to Table VI, one can find here the numerical results (as percentages) used for representing subfigures (j)-(l) in Figs. 4, 5, 6.

TABLE V
Four particular types of general scattering matrices: general form ($\mathbf{S}$), Pauli vector ($\mathbf{k}$) and Real Representation ($\mathbf{S_{RR}}$) particularization.

Type	$\mathbf{S}$	$\mathbf{k}$	$\mathbf{S_{RR}}$
complex symmetric	$\begin{bmatrix} a_1+ia_2 & c_1+ic_2 \\ c_1+ic_2 & b_1+ib_2 \end{bmatrix}$	$\frac{1}{\sqrt{2}}\begin{bmatrix} (a_1+b_1)+i\,(a_2+b_2) \\ (a_1-b_1)+i\,(a_2-b_2) \\ 2\,(c_1+ic_2) \\ 0 \end{bmatrix}$	$\begin{bmatrix} a_1 & c_1 & a_2 & c_2 \\ c_1 & b_1 & c_2 & b_2 \\ a_2 & c_2 & -a_1 & -c_1 \\ c_2 & b_2 & -c_1 & -b_1 \end{bmatrix}$
complex skew-symmetric	$\begin{bmatrix} 0 & -c_1-ic_2 \\ c_1+ic_2 & 0 \end{bmatrix}$	$\frac{1}{\sqrt{2}}\begin{bmatrix} 0 \\ 0 \\ 0 \\ -2i\,(c_1+ic_2) \end{bmatrix}$	$\begin{bmatrix} 0 & -c_1 & 0 & -c_2 \\ c_1 & 0 & c_2 & 0 \\ 0 & -c_2 & 0 & c_1 \\ c_2 & 0 & -c_1 & 0 \end{bmatrix}$
hermitian	$\begin{bmatrix} a_1 & c_1-ic_2 \\ c_1+ic_2 & b_1 \end{bmatrix}$	$\frac{1}{\sqrt{2}}\begin{bmatrix} (a_1+b_1) \\ (a_1-b_1) \\ 2c_1 \\ 2c_2 \end{bmatrix}$	$\begin{bmatrix} a_1 & c_1 & 0 & -c_2 \\ c_1 & b_1 & c_2 & 0 \\ 0 & -c_2 & -a_1 & -c_1 \\ c_2 & 0 & -c_1 & -b_1 \end{bmatrix}$
skew-hermitian	$\begin{bmatrix} ia_2 & c_1+ic_2 \\ -c_1+ic_2 & ib_2 \end{bmatrix}$	$\frac{1}{\sqrt{2}}\begin{bmatrix} i\,(a_2+b_2) \\ i\,(a_2-b_2) \\ 2ic_2 \\ 2ic_1 \end{bmatrix}$	$\begin{bmatrix} 0 & c_1 & a_2 & c_2 \\ -c_1 & 0 & c_2 & b_2 \\ a_2 & c_2 & 0 & -c_1 \\ c_2 & b_2 & c_1 & 0 \end{bmatrix}$

TABLE VI
Real Representation Scattering Matrix eigenvalues type classification, for three elementary targets (orthogonal dihedral, square plate, sphere) displayed for intervals of bistatic angles, $\beta \in [0^o, 90^o]$, with 5^o increment. Incidence directions at $(\theta_i, \varphi_i) = \{(0^o, 0^o), (25^o, 0^o), (40^o, 0^o)\}$.

	Bistatic angles (β) intervals [deg.]																	
	0 - 5	5 - 10	10 - 15	15 - 20	20 - 25	25 - 30	30 - 35	35 - 40	40 - 45	45 - 50	50 - 55	55 - 60	60 - 65	65 - 70	70 - 75	75 - 80	80 - 85	85 - 90
90^o **Dihedral**																		
$(0^o, 0^o)$																		
RR real distinct eigvs. [%]	42.06	89.89	100	100	0	0	0	0	0	0	0	0	0	0	0	0	0	0
RR real equal eigvs. [%]	48.63	5.05	0	0	0	0	0	0	0	0	0	0	0	0	0	0	0	0
RR complex eigvs. [%]	9.3	5.05	0	0	0	0	0	0	0	0	0	0	0	0	0	0	0	0
$(25^o, 0^o)$																		
RR real distinct eigvs. [%]	70.59	61.77	72.73	79.37	74.87	68.23	100	75	100	84	68.96	100	100	60	0	0	0	0
RR real equal eigvs. [%]	24.71	11.63	7.27	4.48	1.47	4.27	0	4.16	0	5.3	17.24	0	0	40	0	0	0	0
RR complex eigvs. [%]	4.7	26.6	20	16.14	23.64	27.5	0	20.83	0	10.6	13.8	0	0	0	0	0	0	0
$(40^o, 0^o)$																		
RR real distinct eigvs. [%]	81.2	50.05	41.47	61.25	71.94	66.52	76.06	56.64	54.53	68.7	70.96	93.7	91.55	96.6	100	81.82	95.24	100
RR real equal eigvs. [%]	6.83	5.5	0	2.28	0.91	9.05	0.77	0.75	2.21	2.53	0	0	0	0	0	7.27	0	0
RR complex eigvs. [%]	11.96	44.44	58.52	36.46	27.15	24.43	23.16	42.61	43.26	28.76	29.1	6.3	8.45	3.3	0	10.91	4.76	0
Square Plate																		0
$(0^o, 0^o)$																		
RR real distinct eigvs. [%]	0.18	1.48	3.36	5.57	9.67	23.1	0	0	0	0	0	0	0	0	0	0	0	0
RR real equal eigvs. [%]	6.91	14.76	31.93	55.55	83.87	76.9	0	0	0	0	0	0	0	0	0	0	0	0
RR complex eigvs. [%]	92.9	83.76	64.71	38.88	6.45	0	0	0	0	0	0	0	0	0	0	0	0	0
$(25^o, 0^o)$																		
RR real distinct eigvs. [%]	0	0	0	7.7	1.11	0.77	2.94	3.15	3.84	0.39	0.23	3.91	10.58	14.75	100	0	0	0
RR real equal eigvs. [%]	0	0	0	76.92	11.07	9.27	25	35.43	38.46	20.51	12.45	44.69	70.58	81.97	0	0	0	0
RR complex eigvs. [%]	0	0	0	15.38	87.82	89.95	72.06	61.42	57.69	79.1	87.31	51.39	18.84	3.28	0	0	0	0
$(40^o, 0^o)$																		
RR real distinct eigvs. [%]	0	0	0	0	0	0	0	0	3.45	4.44	7.25	5.88	5.98	7.69	5.36	1.86	1.38	0
RR real equal eigvs. [%]	0	0	0	0	0	0	0	0	34.48	44.44	57.97	56.86	51.28	53.84	43.45	21.54	13.69	100
RR complex eigvs. [%]	0	0	0	0	0	0	0	0	62.07	51.11	34.78	37.25	42.74	38.46	51.19	76.6	84.92	0
Sphere																		
$(0^o, 0^o)$																		
RR real distinct eigvs. [%]	1.63	1.92	1.83	1.54	1.1	1.1	1.1	1.57	1.36	2.2	0	0	0	0	0	0	0	0
RR real equal eigvs. [%]	4.56	4.26	4.30	4.28	4.53	5.77	5.05	4.63	4.28	3.3	0	0	0	0	0	0	0	0
RR complex eigvs. [%]	93.81	93.82	93.86	94.17	94.37	93.13	93.85	93.8	94.36	94.51	0	0	0	0	0	0	0	0
$(25^o, 0^o)$																		
RR real distinct eigvs. [%]	10.5	2.98	1.81	1	1.01	0.7	1.01	1.05	1.06	0.87	1.07	1.07	2.16	3.07	100	0	0	0
RR real equal eigvs. [%]	25.41	9.14	5.23	3.93	3.16	3.35	4.06	4.2	4.25	4.44	4.51	4.30	3.43	5.52	0	0	0	0
RR complex eigvs. [%]	64.09	87.87	92.95	95.07	95.82	95.95	94.93	94.75	94.7	94.7	94.42	94.62	94.42	91.41	0	0	0	0
$(40^o, 0^o)$																		
RR real distinct eigvs.[%]	21.85	3.77	3.04	2.21	0.64	0.6	0.9	0.86	1.05	1.43	1.83	2.29	1.04	2.5	1.04	2.42	6.6	100
RR real equal eigvs. [%]	38.65	10.61	5.37	3.73	3.84	3.57	4.31	4.47	4.21	3.88	3.47	2.91	4.17	3.33	4.4	2.43	2.92	0
RR complex eigvs. [%]	39.5	85.61	91.58	94.06	95.52	95.82	94.8	94.66	94.74	94.68	94.7	94.80	94.78	94.16	94.56	95.11	90.51	0

ACKNOWLEDGMENT

The authors would like to thank Fabien Ndagijimana from the Grenoble Institute of Technology, Grenoble, France, for providing access to the CST Microwave Studio software.

The authors acknowledge the useful comments and suggestions received from the anonymous reviewers for improving the paper manuscript.

REFERENCES

[1] I. Hajnsek and Y.-L. Desnos, *Polarimetric Synthetic Aperture Radar: Principles and Application*. Springer Nature, 2020.

[2] J.-S. Lee and E. Pottier, *Polarimetric radar imaging: From basics to applications*. CRC Press - Taylor and Francisc Group, 2009.

[3] R. Horn and C. Johnson, *Matrix Analysis - Second Edition*. Cambridge University Press, 2013.

[4] E. Lüneburg, S. Cloude, and W.-M. Boerner, "On the proper polarimetric scattering matrix formulation of the forward propagation versus backscattering radar systems description," in *Proc. IEEE Int. Geosci. Remote Sens. Symp. (IGARSS)*, vol. 4, 1997, pp. 1591–1593.

[5] E. Lüneburg, J. Morisaki, and W.-M. Boerner, "On the forward scatter alignment and the backscatter alignment conventions of bistatic radar polarimetry," in *Proceedings of ISAP*, vol. 1, 2004, pp. 1273–1276.

[6] E. Lüneburg and S. R. Cloude, "Bistatic scattering," in *Wideband Interferometric Sensing and Imaging Polarimetry*, H. Mott and W.-M. Boerner, Eds., vol. 3120, International Society for Optics and Photonics. SPIE, 1997, pp. 56 – 68. [Online]. Available: https://doi.org/10.1117/12.283852

[7] S. Cloude, *Polarisation: Applications in Remote Sensing*. Oxford University Press, Oxford, 2009.

[8] E. Lüneburg and S. R. Cloude, "Radar versus optical polarimetry," in *Wideband Interferometric Sensing and Imaging Polarimetry*, vol. 3120. International Society for Optics and Photonics, 1997, pp. 361–372.

[9] M. Davidovitz and W.-M. Boerner, "Extension of Kennaugh's optimal polarization concept to the asymmetric scattering matrix case," *IEEE Trans. Antennas Propag.*, vol. 34, no. 4, pp. 569–574, 1986.

[10] ——, "Extension of Kennaugh's optimal polarization null theory of the monostatic reciprocal scattering matrix to the bistatic non-symmetrical and/or non-reciprocal monostatic scattering matrix cases," in *Proc. Antennas and Propagation Society International Symp.*, vol. 21, 1983, pp. 484–487.

[11] C. Titin-Schnaider, "Extension of the Huynen theory to bistatic coherent mechanisms," *Proc. of the 3rd International Workshop on Science and Applications of SAR Polarimetry and Polarimetric Interferometry (PolInSAR)*, March 2007.

[12] ——, "Physical meaning of bistatic polarimetric parameters," *IEEE Trans. Geosci. Remote Sens.*, vol. 48, no. 5, pp. 2349–2356, 2010.

[13] ——, "Power optimization for polarimetric bistatic random mechanisms," *IEEE Trans. Geosci. Remote Sens.*, vol. 45, no. 11, pp. 3646–3660, 2007.

[14] L. Bombrun, "Extension of the Target Scattering Vector Model to the bistatic case," in *Proc. IEEE Int. Geosci. Remote Sens. Symp. (IGARSS)*, 2010, pp. 4047–4050.

[15] M. Ciuca, G. Vasile, M. Gay, A. Anghel, and S. Ciochina, "Polarimetric analysis using the algebraic real representation of the scattering matrix," in *Proc. IEEE Int. Geosci. Remote Sens. Symp. (IGARSS)*, 2021, pp. 499–452.

[16] M. Rodriguez-Cassola, P. Prats, U. Steinbrecher, R. Horn, A. Nottensteiner, D. Schulze, M. Keller, M. Pinheiro, M. Zink, A. Reigber, G. Krieger, and A. Moreira, "Bistatic SAR experiments with the TanDEM-X constellation," in *Proc. IEEE Int. Geosci. Remote Sens. Symp. (IGARSS)*, 2012, pp. 1920–1923.

[17] A. Reigber, R. Horn, A. Nottensteiner, P. Prats, R. Scheiber, K.-H. Bethke, and S. Baumgartner, "Current status of DLR's new F-SAR sensor," in *8th European Conference on Synthetic Aperture Radar*, 2010, pp. 1–4.

[18] H. Nies, F. Behner, S. Reuter, O. Loffeld, and R. Wang, "Polarimetric and interferometric applications in a bistatic hybrid SAR mode using TerraSAR-X," in *Proc. IEEE Int. Geosci. Remote Sens. Symp. (IGARSS)*, 2010, pp. 110–113.

[19] ——, "SAR experiments in a bistatic hybrid configuration for generating PolInSAR data with TerraSAR-X illumination," in *8th European Conference on Synthetic Aperture Radar*, 2010, pp. 1–4.

[20] I. Pisciottano, D. Cristallini, D. Pastina, and F. Santi, "Experimental results of polarimetric passive ISAR exploiting DVB-S2 illumination," in *IEEE International Radar Conference*, 2020, pp. 518–523.

[21] A. S. Goh, M. Preiss, N. J. S. Stacy, and D. A. Gray, "The Ingara bistatic SAR upgrade: First Results," in *International Conference on Radar*, 2008, pp. 329–334.

[22] M. Preiss, A. S. Goh, and P. Pincus, "First results from the Ingara L-Band SAR," in *Proc. International Conference on Radar*, 2018, pp. 1–5.

[23] O. A. Krasnov, Z. Wang, F. Van der Zwan, and A. Yarovoy, "A new bistatic radar system: PARSAX + TARA," in *8th European Radar Conference*, 2011, pp. 146–149.

[24] M. Stefko, O. Frey, C. Werner, and I. Hajnsek, "KAPRI: A bistatic full-polarimetric interferometric real-aperture radar system for monitoring of natural environments," in *Proc. IEEE Int. Geosci. Remote Sens. Symp. (IGARSS)*, 2021, pp. 1950–1953.

[25] A. Orban, D. Defrere, and C. Barbier, "BelSAR : The first belgian airborne campaign for L-band, full polarimetric bistatic and interferometric SAR acquisitions over an agricultural site in Belgium," in *13th European Conference on Synthetic Aperture Radar*, 2021, pp. 1–4.

[26] K. A. De Macedo, G. Masalias, A. Coccia, and A. Meta, "Recent L-C- and X-band MetaSensing airborne SAR campaigns for emerging applications," in *17th European Radar Conference*, 2021, pp. 190–193.

[27] A. Liu, F. Wang, H. Xu, and L. Li, "N-SAR: A new multichannel multimode polarimetric airborne SAR," *IEEE J. Sel. Topics Appl. Earth Observ. Remote Sens.*, vol. 11, no. 9, pp. 3155–3166, 2018.

[28] S. Wang, W. Feng, K. Kikuta, G. Chernyak, and M. Sato, "Ground-based bistatic polarimetric interferometric synthetic aperture radar system," in *Proc. IEEE Int. Geosci. Remote Sens. Symp. (IGARSS)*, 2019, pp. 8558–8561.

[29] M. Stefko, S. Leinss, O. Frey, and I. Hajnsek, "Coherent backscatter enhancement in bistatic Ku-/X-band radar observations of dry snow," *The Cryosphere Discussions [preprint]*, vol. 2021, pp. 1–32, 2021. [Online]. Available: https://tc.copernicus.org/preprints/tc-2021-358/

[30] P. López-Dekker, H. Rott, P. Prats-Iraola, B. Chapron, K. Scipal, and E. D. Witte, "Harmony: an Earth Explorer 10 Mission Candidate to observe land, ice, and ocean surface dynamics," in *Proc. IEEE Int. Geosci. Remote Sens. Symp. (IGARSS)*, 2019, pp. 8381–8384.

[31] J. Lopez Dekker, J. Biggs, B. Chapron, A. Hooper, A. Kääb, S. Massina, J. Mouginot, B. Buongiorno Nardelli, and C. Pasquero, "The Harmony mission: applications and preliminary performance," in *6th Workshop on Advanced RF Sensors and Remote Sensing Instruments*, 2019.

[32] T. Li, K.-S. Chen, and M. Jin, "Analysis and simulation on imaging performance of backward and forward bistatic synthetic aperture radar," *Remote Sensing*, vol. 10, no. 11, 2018. [Online]. Available: https://www.mdpi.com/2072-4292/10/11/1676

[33] J. Ding, Z. Zhang, M. Xing, and Z. Bao, "A new look at the bistatic-to-monostatic conversion for Tandem SAR image formation," *IEEE Geosci. Remote Sens. Lett.*, vol. 5, no. 3, pp. 392–395, 2008.

[34] M. Bartusch, A. N. Quiroz, S. Stettner, A. Moreira, and M. Zink, "German X-Band Spaceborne SAR Heritage and the future HRWS Mission," in *Proc. IEEE Int. Geosci. Remote Sens. Symp. (IGARSS)*, 2021, pp. 804–806.

[35] C. Li, H. Zhang, Y. Deng, R. Wang, K. Liu, D. Liu, G. Jin, and Y. Zhang, "Focusing the L-Band spaceborne bistatic SAR mission data using a modified RD algorithm," *IEEE Trans. Geosci. Remote Sens.*, vol. 58, no. 1, pp. 294–306, 2020.

[36] I. Walterscheid, T. Espeter, C. Gierull, J. Klare, A. R. Brenner, and J. H. G. Ender, "Results and analysis of hybrid bistatic SAR experiments with spaceborne, airborne and stationary sensors," in *Proc. IEEE Int. Geosci. Remote Sens. Symp. (IGARSS)*, vol. 2, 2009, pp. II–238–II–241.

[37] M. Rodriguez-Cassola, S. V. Baumgartner, G. Krieger, A. Nottensteiner, R. Horn, U. Steinbrecher, R. Metzig, M. Limbach, P. Prats, J. Fischer, M. Schwerdt, and A. Moreira, "Bistatic

spaceborne-airborne experiment TerraSAR-X/F-SAR: Data processing and results," in *Proc. IEEE Int. Geosci. Remote Sens. Symp. (IGARSS)*, vol. 3, 2008, pp. 451–454.

[38] A. Anghel, R. Cacoveanu, A.-S. Moldovan, B. Rommen, and M. Datcu, "COBIS: Opportunistic C-Band bistatic SAR differential interferometry," *IEEE J. Sel. Topics Appl. Earth Observ. Remote Sens.*, vol. 12, no. 10, pp. 3980–3998, 2019.

[39] A. Anghel, M. Tudose, R. Cacoveanu, M. Datcu, G. Nico, O. Masci, A. Dongyang, W. Tian, C. Hu, Z. Ding *et al.*, "Compact ground-based interferometric synthetic aperture radar: Short-range structural monitoring," *IEEE Signal Process. Mag.*, vol. 36, no. 4, pp. 42–52, 2019.

[40] L. M. Ulander, P.-O. Frölind, A. Gustavsson, and G. Stenström, "Bistatic P-band SAR signatures of forests and vehicles," in *Proc. IEEE Int. Geosci. Remote Sens. Symp. (IGARSS)*, 2012, pp. 311–314.

[41] P. Dreuillet, H. Cantalloube, E. Colin, P. Dubois-Fernandezx, X. Dupuis, P. Fromage, F. Garestier, D. Heuze, H. Oriot, J. Peron, J. Peyret, G. Bonin, O. du Plessis, J. Nouvel, and B. Vaizan, "The ONERA RAMSES SAR: Latest significant results and future developments," in *IEEE Conference on Radar*, 2006, pp. 7 pp.–.

[42] D. Henke, A. Barmettler, and E. Meier, "Bistatic experiment with the UWB-CARABAS sensor - First results and prospects of future applications," in *Proc. IEEE Int. Geosci. Remote Sens. Symp. (IGARSS),*, vol. 2, 2009, pp. II–234–II–237.

[43] E. Gill, W. Huang, and J. Walsh, "The effect of the bistatic scattering angle on the high-frequency radar cross sections of the ocean surface," *IEEE Geoscience and Remote Sensing Letters*, vol. 5, no. 2, pp. 143–146, 2008.

[44] Y. Hong and R. A. Horn, "A canonical form for matrices under consimilarity," *Linear Algebra and its Applications*, vol. 102, pp. 143 – 168, 1988.

[45] C. Graves, "Radar polarization power scattering matrix," *Proceedings of the IRE*, vol. 44, no. 2, pp. 248–252, 1956.

[46] E. Lüneburg and W.-M. Boerner, "Consimilarity classification of general radar scattering matrices," in *Proceedings of ISAP*, Sept., Chiba, Japan 1996, pp. 1041–1044.

[47] W.-M. Boerner, C. Liu, and X. Zhang, "Comparison of optimization procedures for 2x2 Sinclair, 2x2 Graves, 3x3 Covariance, and 4x4 Mueller (symmetric) matrices in coherent radar polarimetry and its application to target versus background discrimination in microwave remote sensing and imaging," *EARSeL Advances in Remote Sensing*, vol. 2, no. 1, pp. 55–82, 1993.

[48] D. Bebbington and L. Carrea, "On Mathematical and Physical Principles of Transformations of the Coherent Radar Backscatter Matrix," *IEEE Trans. Geosci. Remote Sens.*, vol. 50, no. 11, pp. 4657–4669, Nov. 2012.

[49] K. D. Ikramov, "On condiagonalizable matrices," *Linear algebra and its applications*, vol. 424, no. 2-3, pp. 456–465, 2007.

[50] ——, "On the coneigenvalues and singular values of a complex square matrix," *Journal of Mathematical Sciences*, vol. 141, no. 6, pp. 1633–1638, 2007.

[51] M. G. K., "On coneigenvalues of a complex square matrix," *International Journal of Mathematical Modelling & Computations*, vol. 3, no. 3, pp. 253–258, 2013.

[52] S. K. Cho, *Electromagnetic scattering*. Springer Science & Business Media, 2012.

[53] T. Jiang, X. Cheng, and L. Chen, "An algebraic relation between consimilarity and similarity of complex matrices and its applications," *Journal of Physics: Mathematical and General*, vol. 39, pp. 9215–9222, 2006.

[54] T. Jiang and M. Wei, "On the reduction of a complex matrix to triangular or diagonal by consimilarity," *Numerical Mathematics-English Series*, vol. 15, no. 2, p. 107, 2006.

[55] S. Ling and T. Jiang, "New method for general Kennaugh's pseudoeigenvalue equation in radar polarimetry," *Front. Math. China*, vol. 7, no. 1, pp. 85–95, Aug. 2012.

[56] V. t. Karnychev, "Algorithms for estimating the complete group of polarization invariants of the scattering matrix (SM) based on measuring all SM elements," *IEEE Trans. Geosci. Remote Sens.*, vol. 42, no. 3, pp. 529–539, 2004.

[57] O. A. Krasnov and L. P. Ligthart, "Radar polarimetry using sounding signals with dual orthogonality - PARSAX approach," in *The 7th European Radar Conference*, 2010, pp. 121–124.

[58] W. L. Cameron and L. K. Leung, "Feature motivated polarization scattering matrix decomposition," in *IEEE International Conference on Radar*, 1990, pp. 549–557.

[59] L. Iannini, M. Kleinherenbrink, A. Theodosiou, and P. Lopez-Dekker, "Linear principal polarizations in bistatic SAR mission companions," in *Proc. IEEE Int. Geosci. Remote Sens. Symp. (IGARSS)*, 2021, pp. 3073–3076.

[60] E. Kemptner and A. Osipov, "Plane-of-scattering bistatic scattering matrix of simply shaped targets," in *European Conference on Antennas and Propagation (EuCAP)*, 2007, pp. 1–5.

[61] N. Trouve, E. Colin-Koeniguer, P. Fargette, and A. De Martino, "Influence of geometrical configurations and polarization basis definitions on the analysis of bistatic polarimetric measurements," *IEEE Trans. Geosci. Remote Sens.*, vol. 49, no. 6, pp. 2238–2250, 2011.

[62] C. Bradley, P. Collins, J. Fortuny-Guasch, M. Hastriter, G. Nesti, A. Terzuoli, and K. Wilson, "An investigation of bistatic calibration techniques," *IEEE Trans. Geosci. Remote Sens.*, vol. 43, no. 10, pp. 2185–2191, 2005.

[63] R. Kell, "On the derivation of bistatic RCS from monostatic measurements," *Proceedings of the IEEE*, vol. 53, no. 8, pp. 983–988, 1965.

[64] C. J. Bradley, P. J. Collins, D. G. Falconer, J. Fortuny-Guasch, and A. J. Terzuoli, "Evaluation of a near-field monostatic-to-bistatic equivalence theorem," *IEEE Trans. Geosci. Remote Sens.*, vol. 46, no. 2, pp. 449–457, 2008.

[65] K. Wilson, "Method for predicting the maximum reliable angle to use in the monostatic-to-bistatic equivalence theorem," *IEEE Antennas Propag. Mag.*, vol. 43, no. 3, pp. 108–111, 2001.

[66] G. J. Tee, "Eigenvectors of block circulant and alternating circulant matrices," *New Zealand Journal of Mathematics*, vol. 36, no. 8, pp. 195–211, 2007.

[67] E. Lüneburg and W.-M. Boerner, "Homogeneous and inhomogeneous Sinclair and Jones matrices," in *Wideband Interferometric Sensing and Imaging Polarimetry*, vol. 3120. International Society for Optics and Photonics, 1997, pp. 45–54.